



1 *Research article*

2 **Automated riverbed material analysis using Deep Learning on** 3 **underwater images**

4 Alexander A. Ermilov¹, Gergely Benkő¹ and Sándor Baranya¹

5 ¹Department of Hydraulic and Water Resources Engineering, Budapest University of Technology and Economics,
6 Budapest, 1111, Hungary

7 *Correspondence to:* Alexander A. Ermilov (ermilov.alexander@emk.bme.hu)

8 **Abstract.** The sediment of alluvial riverbeds plays a significant role in river systems both in engineering and
9 natural processes. However, the sediment composition can show great spatial and temporal heterogeneity, even
10 on river reach scale, making it difficult to representatively sample and assess. Indeed, conventional sampling
11 methods in such cases cannot describe well the variability of the bed surface texture due to the amount of energy
12 and time they would require. In this paper, an attempt is made to overcome this issue introducing a novel image-
13 based, Deep Learning algorithm and related field measurement methodology with potential for becoming a
14 complementary technique for bed material samplings and significantly reducing the necessary resources. The
15 algorithm was trained to recognise main sediment classes in videos that were taken underwater in a large river
16 with mixed bed sediments, along cross-sections, using semantic segmentation. The method is fast, i.e., the videos
17 of 300-400 meter long sections can be analysed within minutes, with very dense spatial sampling distribution. The
18 goodness of the trained algorithm is evaluated mathematically and via intercomparison with other direct and
19 indirect methods. Suggestions for performing proper field measurements are also given, furthermore, possibilities
20 for combining the algorithm with other techniques are highlighted, briefly showcasing the multi-purpose of
21 underwater videos for hydromorphological adaptation. The paper is to show the potential of underwater
22 videography and Deep Learning through a case study.

23 **Keywords:** rivers, sedimentology, mapping, Artificial Intelligence, Deep Learning, underwater, image-based

24 **1 Introduction**

25 The physical composition of a riverbed plays a crucial role in fluvial hydromorphological processes, as a sort of
26 boundary condition in the interaction mechanisms between the flow and the solid bed. Within these processes, the
27 grains on the riverbed are responsible for multiple phenomena, such as flow resistance (Vanoni and Hwang, 1967;
28 Zhou et al., 2021), stability of the river bed (Staudt et al., 2018; Obodovskyi et al., 2020), development of bed
29 armour (Rákóczi, 1987; Török et al., 2017), sediment clogging (Rákóczi, 1997; Fetzer et al., 2017), fish shelter
30 (Scheder et al., 2015), etc. Through these physical processes, the bed material composition has a determining
31 effect on numerous river uses, e.g., possibilities of fluvial navigation, drinking water supply through bank
32 filtration, the quality of riverine habitats, etc. Knowledge of riverbed structure and grain composition is therefore
33 of major importance in river hydromorphology. In order to gain information about river bed sediments, *in situ*
34 field sampling methodologies are implemented.

35



36 Traditionally, bed material sampling methods are intrusive (i.e., sediment is physically extracted from the bed for
37 follow-up analysis) and carried out via collecting the sediment grains one-by-one (areal, grid-by-number and
38 pebble count methods, see e.g., Bunte and Abt, 2001; Guerit et al., 2018) or in a larger amount by a variety of
39 grab samplers (volumetric methods, such as WMO, 1981; Singer, 2008). This is then followed by measuring their
40 sizes individually on-site or transporting them to a laboratory for mass-sieving analysis (Kellerhals and Bray,
41 1971; Fehr, 1987; Diplas, 1988; Bunte and Abt, 2001). These sampling procedures are time- and energy
42 consuming, especially in large gravel and mixed bed rivers, where characteristic grain sizes can strongly vary both
43 in time and space (Church et al., 1987; Wolcott and Church, 1991; Rice and Church, 1998; USDA, 2007),
44 requiring a dense sampling point allocation. The same goes for critical river reaches, where significant human
45 impact led to severe changes in the morphological state of the rivers (e.g., the upper-section of the Hungarian
46 Danube; Török and Baranya, 2017). When assessing bed material composition on a river reach scale, experts
47 usually try to extrapolate from the samples, and describe larger regions of the bed (even several thousand m²) by
48 data gathered in a few, several dozen points (see e.g., USDA, 2007; Haddadchi et al., 2018; Baranya et al., 2018;
49 Sun et al., 2021). Gaining a representative amount of the sediment samples is also a critical issue. For instance,
50 following statistical criteria such as those of Kellerhals and Bray (1971) or Adams (1979), a representative sample
51 should weigh ten-to-hundred kg. Additionally, physical bed material sampling methods are unable to directly
52 quantify important, hydromorphological features such as roughness or bedforms (Graham et al., 2005). Due to
53 these constraints, surrogate approaches have recently been intensively tested to analyse the riverbed (see Chapter
54 2). Unlike the conventional methods, these techniques are non-intrusive and rely on computers and other
55 instrumentation to decrease the need of human intervention and speed up the analyses. The goal of this paper is
56 to introduce a Deep Learning-based technique and its first set of results which shows potential in complementing
57 the traditional methods, while also providing broader knowledge of the riverbed than before through improved
58 (continuous, quick, covering larger areas) data collection. First, a literature review is given to better understand
59 the current state of surrogate approaches and their research, gradually leading up to the method of this paper and
60 highlighting its relevance. In the third chapter the case studies and the methodology are introduced in details. The
61 third chapter presents the results and their evaluation, followed by a discussion about the challenges, the novelty
62 and possible continuations of the method. A brief discussion is also given on how the method can support
63 traditional methods and what kind of additional hydromorphological parameters can be provided by such videos,
64 uniquely improving the toolkits of sedimentation engineering. Finally, the main conclusions of the paper are
65 drawn.

66 **2 Literature review**

67 One group of the surrogate approaches is the acoustic methods, where an acoustic wave source (e.g., an Acoustic
68 Doppler Current Profiler; ADCP) is pointed towards the riverbed from a moving vessel, emitting a signal. The
69 strength and frequency of this signal is measured while it passes through the water column, reflecting back to the
70 receiver from the sediment transported by the river, and finally from the riverbed itself. This approach is fast and
71 larger areas can be covered relatively quickly (Guerrero and Lamberti, 2011; Grams et al., 2013). While it has
72 already become widely used for describing movement (i.e., suspended sediment, bedload and indirectly flow
73 velocity; Shields and Rigby, 2005; Guerrero et al., 2016; Muste et al., 2016) and channel shape (Zhang et al.,
74 2008), it has not reached similar breakthrough for riverbed material analysis. Researchers found that it is necessary



75 to apply instrument specific coefficients to convert the signal strength, and these coefficients can only be derived
76 by first validating each instrument using collected sediment samples with corresponding ADCP data. Moreover,
77 the method is sensitive to the bulk density of the sediment and to bedforms (Shields, 2010), while it is also not
78 possible to measure individual grains this way (Buscombe et al., 2014a; 2014b). Hence, the separation of surface
79 roughness from the effects of bedforms is also not possible. Clay and silt patches could be separated with the
80 acoustic approach, but gravel could not be distinguished strongly from sand.

81

82 Another group of the surrogate approaches is the application of photography (Kellerhals and Bray, 1971; Adams,
83 1979; Ibbekken and Schleyer, 1986) and later computer vision or image-processing techniques. During the last
84 two decades, two major subgroups emerged: one uses object- and edge detection (by finding abrupt changes in
85 intensity and brightness of the picture, segmenting objects from each other; Butler et al., 2001; Sime and Ferguson,
86 2003; Detert and Weitbrecht, 2013), and the other one analyses the textural properties of the whole image, using
87 autocorrelation and semi-variance methods to define empirical relationship between image texture and the grain
88 sizes of the photographed sediments (Carbonneau et al., 2004; Rubin, 2004; Verdú et al., 2005). The above-
89 mentioned image processing approaches were very time consuming and required mostly site-specific manual
90 settings, however, a few transferable and more automated techniques have also been developed recently (e.g.,
91 Graham et al., 2005; Buscombe, 2013). Even though there is a continuous improvement in the applied image-
92 based bed sediment analysis methods, there are still major limitations the users face with, such as:

93

- 94 • Most of the studies (all the ones listed above) focuses on gravel bed rivers, and only a few exceptions
95 can be found in the literature where sand is also accounted for (texture-based methods; Chezar and
96 Rubin, 2004; Buscombe and Masselink, 2008; Warrick et al., 2009; Buscombe, 2013).
- 97 • The adaptation environment was typically non-submerged sediment, instead of underwater
98 conditions (a few exceptions: Chezar and Rubin, 2004; Warrick et al., 2009).
- 99 • The computational demand of the image processing is high (e.g., one to ten minutes per image;
100 Detert and Weitbrecht, 2013; Purinton and Bookhagen, 2019).
- 101 • The analysis requires operator expertise (higher than in case of any conventional method).
- 102 • There is an inherent pixel- and image resolution limit (Graham et al., 2005; Buscombe and
103 Masselink, 2008; Buscombe, 2013; Cheng, 2015; Purinton and Bookhagen, 2019). The finer the
104 sediment, the higher resolution of the images should be (higher calculation time), or they must be
105 taken from a closer position (smaller area and sample per image).
- 106 • Due to the limitations above, most of the methods enable the analysis of smaller areas (in the order
107 of $\sim 10 \text{ m}^2$) only and are not applicable for quick, continuous measurements of larger regions.

108

109 Nowadays, with the rising popularity of Artificial Intelligence (AI), several Machine Learning (ML) techniques
110 have been implemented in image recognition as well.

111

112 The main approaches of segmentation contra textural analysis still remain; however, an AI defines the empirical
113 relationship between the object sizes (Igathinane et al., 2009; Kim et al., 2020) or texture types (e.g., Buscombe
114 and Ritchie, 2018) in the images and their real sizes. In the field of river sedimentology a few examples can



115 already be found, where ML (e.g., Deep Learning; DL) was implemented. For instance, Rozniak et al. (2019)
116 developed an algorithm for gravel-bed rivers, performing textural analysis. With this approach, individual grains
117 are not detected, but rather the general grain size distribution (GSD) of the whole images. At certain points of the
118 studied river basins, conventional physical samplings (pebble count) were performed to provide real GSD
119 information. Using this data, the algorithm was trained (with ~1000 images) to estimate GSD for the rest of the
120 study site, based on the images. The method worked for areas where grain diameters were larger than 5 mm, and
121 the sediment was well-sorted. The developed method showed sensitivity to sand coverage, blurs, reduced
122 illuminations (e.g., shadows) and white pixels. Soloy et al. (2020) presented an algorithm which used object
123 detection on gravel- and cobble covered beaches to calculate individual grain sizes and shapes. Approximately 50
124 images were used for the model training, however, the number of images were multiplied with data augmentation
125 (rotating, cropping, blurring the images; see Perez and Wang, 2017) to enhance the learning session and increase
126 the input data. The method was able to reach a limited execution speed of a few seconds per m² and adequately
127 measured the sizes of gravels. Ren et al. (2020) applied an ensemble bagging-based Machine Learning (ML)
128 algorithm to estimate GSD along the 70 km long Hanford Reach of the Columbia river. Due to its economic
129 importance, a large amount of measurement data has been accumulated for this study site over the years, making
130 it ideal for using ML. By the time of the study, 13,372 scaled images (i.e., their millimetre/pixel ratio was known)
131 were taken both underwater and in the dry zones, covering approx. 1 m² area each. The distance between the
132 image-sampling points was generally between 50-70 m. An expert defined the GSD (8 sediment classes) of each
133 image by using a special, visual evaluation-classification methodology (Bovee, 1982, Delong and Brusven, 1991;
134 Geist et al., 2000). This dataset was fed to a ML algorithm along with their corresponding bathymetric attributes
135 and hydrodynamic properties, simulated with a 2D hydrodynamic model. Then, it was tested to predict the
136 sediment classes based on the hydrodynamic parameters only. The algorithm performed with a mean accuracy of
137 53%. Even though this method was not image-based (only indirectly, via the origin of the GSD data), it highlighted
138 the possibilities of an AI for a predictive model, using a high-dimensional dataset. Having such a large data of
139 grain size information can be considered exceptional and takes a huge amount of time to gather, even with the
140 visual classification approach they adapted. Moreover, this was still considered spatially sparse information
141 (point-like measurements, 1 m² covered area/image dozens of meters away from each other). Buscombe (2020)
142 used a set of 400 scaled images to train a DL algorithm on image texture properties, using another image-
143 processing method (Barnard et al., 2007) for validation. The algorithm reached a good result for not only gravel,
144 but sand GSD calculation as well, outperforming an earlier, but promising, texture-based method (wavelet
145 analysis; Buscombe, 2013). In addition, the method required fewer calibration parameters than the wavelet image-
146 processing approach. The study also foresaw the possibility to train an AI which estimates the real sizes of the
147 grains, without knowing the scale of one pixel (mm/pixel ratio) if the training is done properly. The AI might
148 learn unknown relationships between the texture and sizes if it is provided with a wide variety (images of several
149 sediment classes) and scale (mm/pixel ratio) of dataset (however, it is also prone to learn unwanted biases).
150 Recently, Takechi et al. (2021) further elaborated on the importance of shadow- detection and removal, using a
151 dataset of 500 pictures for training a texture-based AI, with the help of an object-detecting image-processing
152 technique (Basegrain; Detert and Weitbrecht, 2013).

153



154 The previously presented studies, applying ML and DL techniques, significantly contributed to the development
155 and improvement of surrogate sampling methods, incorporating the great potential in AI. However, there are still
156 several shortcomings to these procedures. Firstly, none of the image-based DL studies used underwater recordings,
157 even though the underwater environment offers completely different challenges. Secondly, the training images
158 were always scaled, i.e., the sizes of the grains could be easily reconstructed, which is again complicated to
159 accomplish in a river. Lastly, they were not adapted for continuous measurement, but rather focused on a grid-
160 like approach.

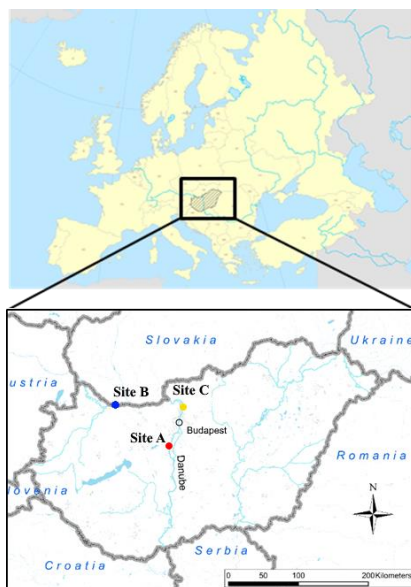
161

162 The method introduced in this paper follows the ML and DL approach as well. The main novelty of our DL and
163 measurement method, however, is that both the training and analysed videos are recorded underwater,
164 continuously along cross-sections of a large river. Furthermore, the training is unscaled, i.e., the camera-riverbed
165 distance could vary while recording the videos, without considering image-scale. Moreover, compared to the
166 relatively low number of training images in most of the above referred studies, we used a very large dataset
167 (~15000) of sediment images for the texture-based AI, containing mostly: sand, gravel, cobble, and to a smaller
168 extent: bedrock together with some other, non-sediment related objects.

169 3 Methods

170 3.1 Case studies

171 The results presented in this study are based on riverbed videos taken during three measurement campaigns, in
172 sections of the Danube river, Hungary. The first one was at Site A, Ercsi settlement (~ 1606 rkm), the second one
173 was at Site B, Gönyű settlement (~ 1791 rkm), and the third was at Site C, near to Göd settlement (~ 1667 rkm)
174 (Fig. 1).



175
176
177

Figure 1: The location of the riverbed videos, where the underwater recordings took place (upper section of the Hungarian Danube).



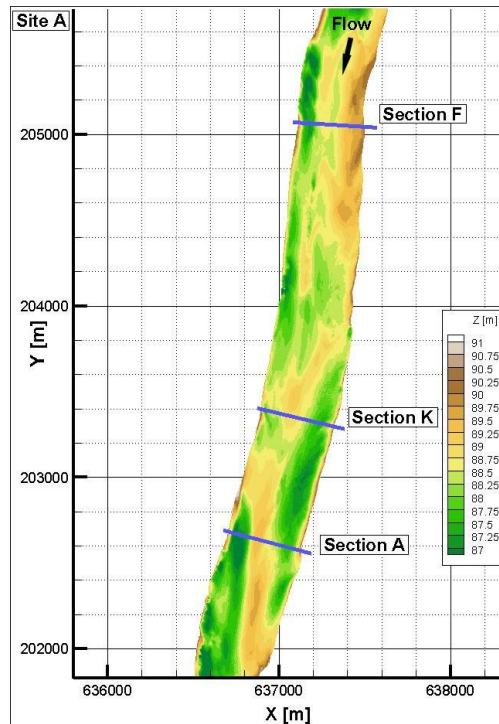
178 The training of the AI was done using the video images of Site C and a portion of A (test set; see later in Chapter
 179 3.3), while Site B and the rest of the images from A served for validation. The measurements were carried out
 180 during daytime, at mid-water regime ($Q = 1900 \text{ m}^3/\text{s}$) in case of Site A, and low water regime ($Q = 1350 \text{ m}^3/\text{s}$) at
 181 Site B, similarly to Site C ($Q = 700 \text{ m}^3/\text{s}$). This latter site served only for increasing the training image dataset
 182 (i.e., conventional samplings were not carried out at the time of recording the videos), thus we do not go into
 183 further details with it for the rest of the paper, but the main characteristics are listed in Table 1. As underwater
 184 visibility conditions are influenced by the suspended sediment, the characteristics of this sediment transport is
 185 also included in Table 1 (Q_{susp} - susp. sed. load; SSC – susp. sed. concentration).

186

	Site A	Site B	Site C
Q [m³/s]	1900	1350	700
B [m]	300 – 450		
H_{mean} [m]	3.5 - 4.5		
S [cm/km]	15		
Characteristic sediment	riverbed gravel, sandy gravel	gravel, gravelly sand	gravel, sandy gravel
Q_{annual,av} [m³/s]	2000	2200	1400
SSC [mg/l]	25	20	14

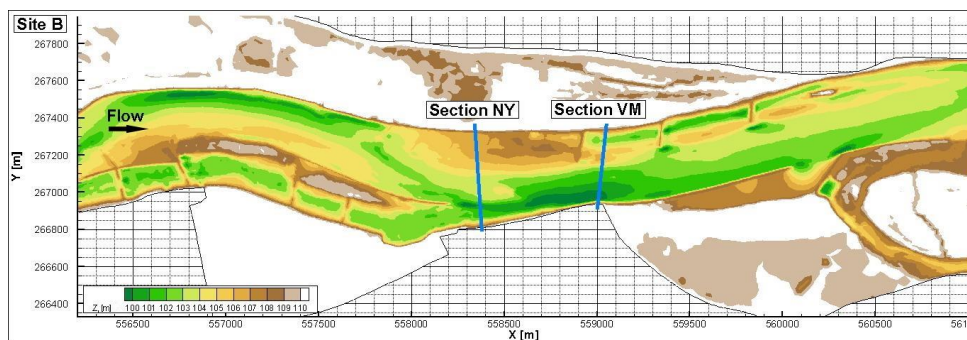
187 **Table 1: Main hydromorphological parameters of the measurement sites. Q: discharge during survey; B: river width;**
 188 **H_{mean}: mean water depth during the survey; S: river bed slope; Q_{annual, av.}: annual-average of the discharge at the site;**
 189 **SSC: average suspended sediment concentration during the survey.**

190 The highest water depths were around 6-7 m in all cases. In Site A, measurements included mapping of the
 191 riverbed with a camera along three separate transects (Fig.2). At Site B, two transects were recorded (Fig.3).



192
193 **Figure 2:** At Site A, three transects were measured. The vessel moved along these lines from one bank to the other,
194 while carrying out ADCP measurement and recording riverbed videos. Physical bed material samples were also
195 collected in certain points of these sections.

196



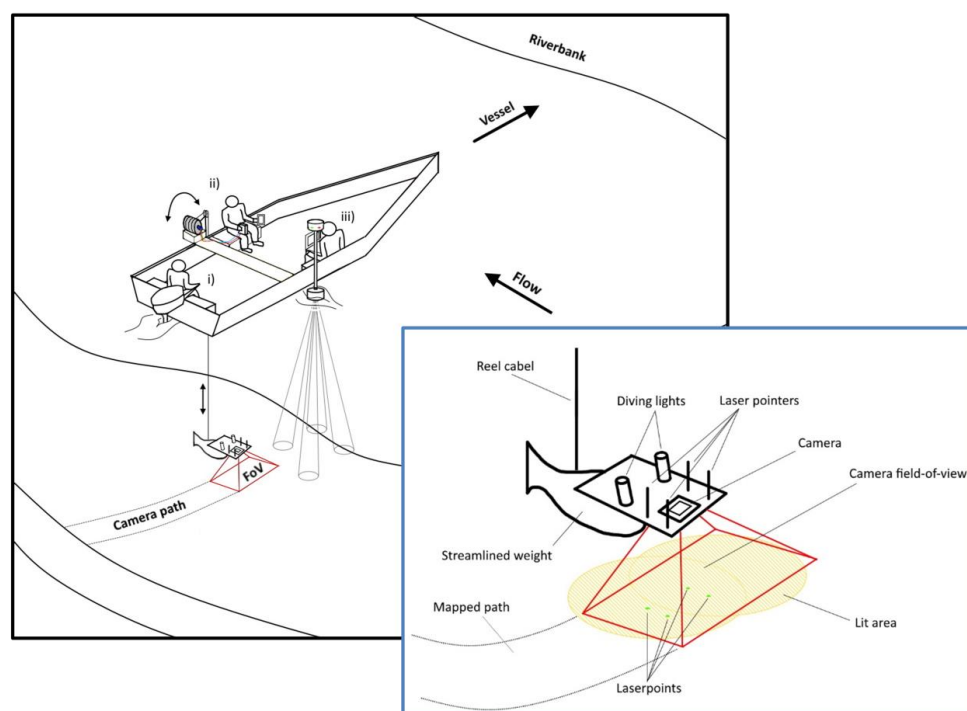
197
198 **Figure 3:** At Site B, two transects were measured. The vessel moved along these lines from one bank to the other,
199 while carrying out ADCP measurement and recording riverbed videos. Physical bed material samples were also
200 collected in certain points of these sections.

201 3.2 Field data collection

202 Figure 4 presents a sketch of the measurement process with the equipment and a close-up of the underwater
203 instrumentation. During the field measurements, the camera was attached to a streamlined weight and lowered
204 into the water from the vessel by an electric reel. The camera was positioned perpendicularly to the water and the
205 riverbed, in front of the nose of the weight. Next to the camera, two diving lights worked as underwater light
206 sources, focusing into the camera's field of view (FoV). In addition, four laser pointers were also equipped in



207 hand-made isolation cases to provide possible scales for secondary measurements. They were also perpendicular
208 to the bottom, projecting their points onto the underwater camera field of view. Their purpose was to ensure a
209 visible scale (mm/pixel ratio) in the video footages for validation. During the measurement procedure, a vessel
210 crossed the river slowly through river transects, while the position of the above detailed equipment was constantly
211 adjusted by the reel. Simultaneously, ADCP and RTK GPS measurement were carried out by the same vessel,
212 providing water depth, riverbed geometry, flow velocity, ship velocity and position data. Based on this information
213 and by constantly checking the camera's live footage on deck, the camera was lowered or lifted to keep the bed
214 in camera sight, and avoid colliding with it. The vessel's speed was also adjusted based on the video and slowed
215 down if the video was blurry or the camera got too far away from the bed (see later in Chapter 4.3). The
216 measurements required three personnel to i) drive the vessel, ii) handle the reel, adjust the equipment position,
217 and monitor the camera footage, iii) monitor the ADCP data, while communicating with the other personnel (see
218 Fig. 4).



219 **Figure 4:** Left: sketch of the measurement process. The vessel was moving perpendicular to the riverbank along a cross-
220 section (i). A reel was used to lower a camera close to the riverbed (ii). Simultaneously, the bed topography and water
221 depth were measured by an ADCP (iii). Right: Close-up sketch of the underwater instrumentation.

223 The video recordings were made with a GOPRO Hero 7 and a Hero 4 commercial action cameras. Image
224 resolutions were set to 2704x2028 (2.7K) with 60 frame per second (fps) and 1920x1080 (1080p) with 48 fps,
225 respectively. Other parameters were left at their default (see GOPRO 2014; 2018), resulting in slightly different
226 quality of produced images between the two cameras. Illumination is a critical condition for riverbed imaging.
227 Here, a diving light with 1500 lumen brightness and 75° beam divergence, and one with 1800 lumen and 8° were



228 used. The four lasers for scaling had 450-520 nm (purple and green) wavelength and 1-5 mW nominal power.
229 Power supply was ensured with batteries for all instruments.

230
231 At Site A and Site B, conventional bed material (physical) samplings were also carried out by a grabbing (bucket)
232 sampler along the analysed transects. At each cross-section had 4-5 samples were taken. The collected samples
233 were analysed in laboratory by drying, sieving, and weighing to provide local grain size distribution. The measured
234 GSDs were used to validate results of the AI algorithm. Separately, a visual evaluation of the videos was also
235 carried out, where a person divided the transects into subsections based on their dominant sediment classes, after
236 watching the footages.

237 **3.3 Image analysis: Artificial Intelligence and the wavelet method**

238 A widely used deep neural network architecture was employed in this study, building on former experiences of
239 the authors (Benkó et al., 2020), Google's DeeplabV3+ Mobilnet, in which many novel and state-of-the-art
240 solutions are implemented (e.g., Atrous Spatial Pyramid Pooling; Chen et al., 2018). The model was implemented
241 with Pytorch, exploiting its handy API and backward compatibility. The main goal was to build a deep neural
242 network model which is able to recognise and categorise (via semantic segmentation; Chen et al., 2018) at least
243 three main sediment size classes, i.e., sand, gravel and cobble, in the images, while being quickly deployable. The
244 benefit of the introduced method compared to conventional imagery methods lies in the potential of automation
245 and increased speed. If the annotation and training is carried out thoroughly, analysing further videos can run
246 effortlessly, while the computation time can be scaled down either vertically (using stronger GPUs) or horizontally
247 (increasing the number of GPUs; if parallel analysis of images is desired). In this study a TESLA K80 24GB
248 GDDR5 348bit GPU, an Intel Skylake Intel® Xeon® Gold 6144 Processor (24.75M Cache, 3.50 GHz) CPU with
249 13GB RAM was used. Also, contrary to other novel image-processing approaches in riverine sediment research
250 (Buscombe, 2013; Detert and Weitbrecht, 2013), the deep convolutional neural network is much less limited by
251 image resolution and mm/pixel ratios, because it does not rely on precise pixel count. This is an important
252 advantage to be exploited here, as we perform non-scaled training and measurements with the AI, i.e., camera-
253 bed distance constantly changed and size-reference was not used in the images.

254
255 The first step in the analysis was to cut the captured videos into frames, during which the videos were exploded
256 into sequential images. Brightening and sharpening filters were applied on the images to improve their quality.
257 Next, the ones with clearest outlines and best visibility were chosen. This selection process was necessary because
258 this way the delineation process (learning the prominent characteristics of each class) can be executed accurately,
259 without the presence of misleading or confusing images, e.g., blurry or dark pictures where the features are hard
260 to recognise. For training purposes, we chose three footages from different sections each being ~15 minutes long
261 with 60 fps and 48 fps, resulting in 129 600 frames. In fact, no such large dataset was needed due to the strong
262 similarity of the consecutive frames. The number of images to be annotated and augmented were therefore
263 decreased to ~2000.

264
265 We also performed a white balance correction on some of the images to improve visibility, making it even easier
266 to later define the sediment class boundaries. We used an additional algorithm to generate more data, with the so-



267 called Simplest Colour Balance method (Limare et al., 2011). It is a simple, but powerful histogram equalisation
268 algorithm which helps to equalise the roughness in pixel distribution.

269

270 These steps were followed by the annotation, where we distinguished ten classes. Annotation was performed with
271 the help of an open-source software called PixelAnnotationTool (Breheret, 2017), which enables the user to colour
272 mask large parts of an image based on colour change derivatives (i.e., colour masking part of the images which
273 belong to the same class, e.g., purple/red – sand, green – gravel, yellow – cobble, etc.). The masks and outlines
274 were drawn manually, together with the so called watershed annotation. That is, when a line was drawn, the
275 algorithm checked for similar pixels in the vicinity and automatically annotated them with the same class. The
276 annotation was followed by a data augmentation step where beside mirroring, cropping, rotating the images (to
277 decrease the chance of overfitting), we also convolved them with different filters. These filters added normally
278 distributed noise to the photos to influence the watershed algorithm and applied sharpening, blurring, darkening,
279 and white balance enhancement. Thus, at the data level, we tried to ensure that any changes in water purity, light,
280 and transparency, as well as colour changes, were adequately represented during training. Images were uniformly
281 converted to 960x540 resolution, scaling them down to make them more usable to fit in the GPU's memory. The
282 next step was to convert all the images from RGB (Red-Green-Blue) based colour to grayscale. This is important
283 because colour images have 3-channels, so that they contain a red, a green, and a blue layer, while grayscale
284 images' pixel can only take one value between 0 and 255. With this colour conversion we obtained a threefold
285 increase in computational speed. In total, a dataset of 14,784 images was prepared (from the ~2000 images of the 4
286 training videos). The next step was to separate this into training and validation sets. In this study, approximately
287 80% of the data was used for training the Artificial Intelligence, while 20% was to validate the training. It was
288 important to mix the images so that the algorithm selects batches in a pseudorandom manner during training, thus
289 preventing the model from being overfitted. Finally, after several changes in the hyperparameters, the evaluation
290 and visualisation of the training results were performed. Learning rate was initialised to 0.01, with 30000 iteration
291 steps, and the learning rate is reset after every 5000 iterations with a decay of 0.1. A batch size of 16 was used.
292 We used a cross-entropy loss function.

293

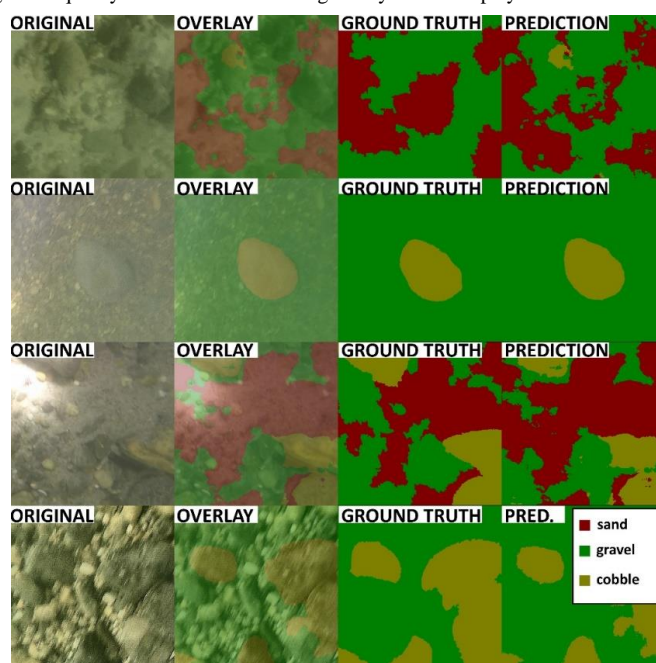
294 As previously mentioned, laser pointers were used to provide scale for the recorded videos, as a secondary
295 validation. We used a textural image-processing method to analyse the video images of the spots, where the
296 physical samples were taken. For this, the already mentioned, transferable wavelet-based signal- and image-
297 processing method (Buscombe, 2013) was chosen. The method enables to calculate the image-based grain size
298 distribution of the selected pictures. The grey-scale intensity is analysed through pixel-rows and -columns of the
299 image and handled as individual signals. Then, instead of Fourier-transform, the less-constrained wavelet-
300 transform is applied to decompose them. Finally, calculating the power spectra and the sizes (from pixel to
301 millimetre, using the scale) of the wavelet components (each wavelet describes an individual grain) produces the
302 grain size distribution for the given image. Beforehand, this method was proved to be the most efficient, non-AI
303 image-processing method for mixed sediments (Buscombe, 2013; 2020) and was already tested for underwater
304 circumstances in an earlier study by the authors of present paper (Ermilov et al., 2020).



305 **4 Results and discussion**

306 **4.1 Evaluation of the training**

307 To evaluate the training process, the image series used for the training was analysed by the developed Deep
308 Learning algorithm. Figure 5. shows results of original images (from the validation set), their ground truth
309 (annotation by the training personnel), as well as the AI prediction (result of the model). The overlays of the
310 original and the predicted images are also shown for better visualization. Calculating the over-all *pixel accuracy*
311 (i.e., the percent of pixels that were correctly classified) returned a satisfactory result with an average 96% match.
312 As this parameter in object detection and Deep Learning is not a stand-alone parameter (i.e., it can still be high
313 even if the model performs poorly), the mean IoU (intersection-over-union or Jaccard index) was also assessed,
314 indicating the overlap of ground truth area and prediction area, divided by their union (Rahman and Wang, 2016).
315 This parameter showed a much slighter agreement of 41.46%. Interestingly, there were many cases, where the
316 model gave better result, than the annotating personnel. The first row of Figure 5. showcases two examples for
317 this: i) the correct appearance of cobble (yellow) in the prediction, even though the user (ground truth) did not
318 define it during the training; ii) correctly sensing gravel in the middle of the image, contrary to a whole sand (red)
319 patch in the ground truth image. As a matter of fact, these positive errors also decrease the IoU evaluation
320 parameter, even though they increase the performance of the AI on the long term. Hence, this shows that pure
321 mathematical evaluation may not describe the model performance entirely. Considering that others also reported
322 similar experience with Deep Learning (Lu et al., 2018) and the fact that 40% and 50% are generally accepted
323 IoU threshold values (Yang et al., 2018; Cheng et al., 2018; Padilla et al., 2020), we considered the 41.46%
324 acceptable. The general quality of our underwater images may have also played a role in lowering the IoU result.



325
326 **Figure 5: Example comparisons of ground truth (taught) and AI predicted (learnt) sediment classes from the training**
327 **videos showing satisfactory results.**



328 **4.2 Intercomparison of methods**

329 In each masked image, the occurring percentage of the given class (i.e., the percentage of the pixels belonging to
330 that class/colour mask, compared to the total number of pixels in the image) was calculated and used as the fraction
331 percentage in that given sampling point. These sediment classes reconstructed by the AI were then compared to
332 three alternative results: i) visual estimation, ii) GSD resulted from conventional grab sampling, iii) wavelet-based
333 image-processing. In the followings, results from two cross-sections will be shown, one from Site A, the video
334 used for the training, and one from Site B, being new for the AI. An averaging window of 15 m was applied on
335 each cross-sectional AI result to smoothen and despike the dataset.

336

337 In Figure 6, the path of the vessel can be seen in Section K, at Site A. The path was coloured based on the visual
338 evaluation of the riverbed images. The different colours represent the dominant sediment type seen at the given
339 point of the bed. The locations of the physical bed material samplings are also shown (see yellow markers). Figure
340 7 shows the cross-sectional visual classification compared to the AI-detected sediment fractions in percentage.

341

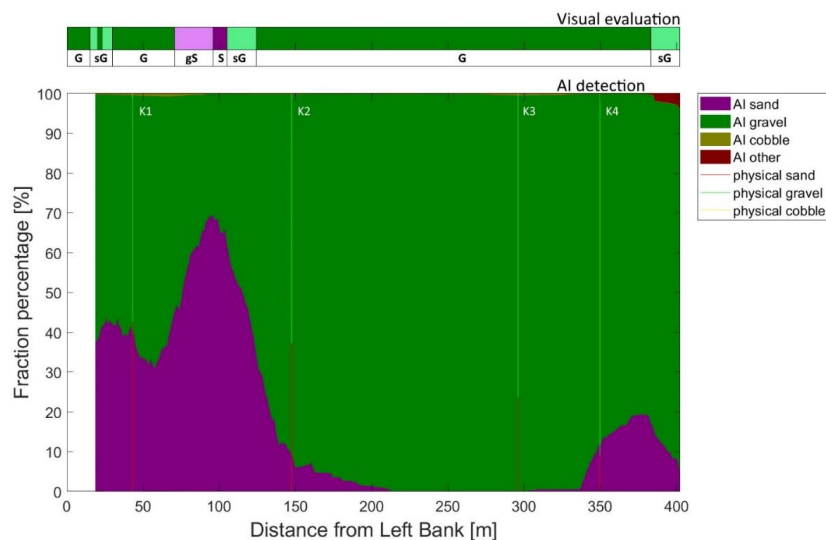


342

343 **Figure 6: The path of the vessel and camera in Section K, Site A. The polyline is coloured based on the sediment features**
344 **seen during visual evaluation of the video. Yellow markers are the locations of physical bed material samplings. (Map**
345 **created with © Google Earth Pro)**



346



347
348
349
350

Figure 7: Section K. The visual evaluation of the dominant sediment features in the video (top) compared to sediment fraction percentage, recognised by the AI (bottom). The visual evaluation included four classes: gravel – G, sandy gravel – sG, gravelly sand – gS, sand – S,). The fractions from the physical samples are also shown (verticals).

351
352
353
354
355
356

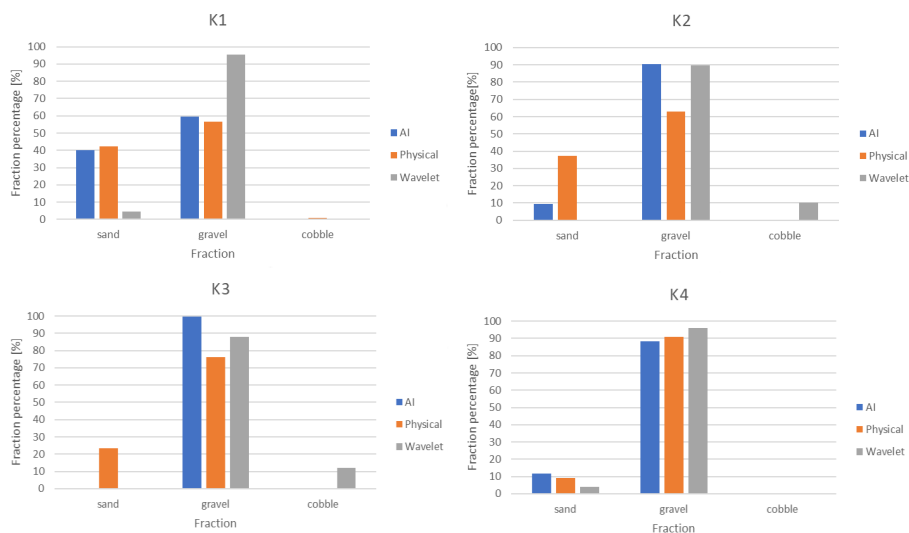
Comparing the two figures, the AI result show satisfactory match with the human evaluation. For example, around 100 m from the left bank, between K1 and K2 sampling points, the AI peaks with around 70% sand an 30% gravel correctly. Furthermore, on the two side of this peak a steep transition to gravel and decreasing sand occurs, similarly to the eye observation, marked as sandy gravel and gravelly sand. Mixed sediment zones were also correctly identified by the AI at both riverbanks.

357
358
359
360
361
362
363
364
365
366
367
368
369
370
371

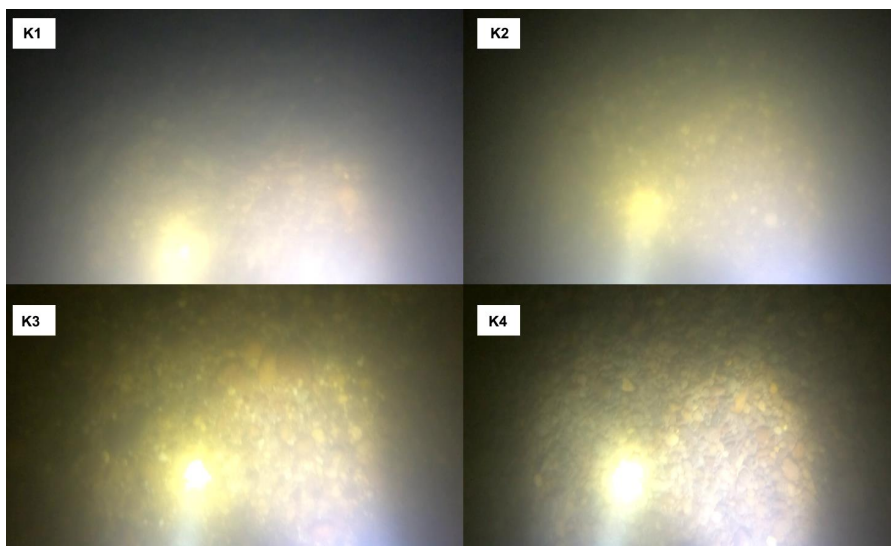
Next, the AI estimated sediment classes were compared with both the physical samples and the wavelet method at each sampling locations (Fig. 8). The images of the bed from the sampling points are in shown in Figure 9. As for the AI results, a moving average-based smoothing was applied in the 15 m vicinity of the sampling locations. Overall, the AI based classification agrees well with the physical samples, however, at sample K3 the ~20% sand content was neither reconstructed by the AI, nor could be observed by eye (see Fig. 9). Considering that the gravel dominates the bed sediments, the absence of sand fraction in the AI results might be explained with the difference between the surface GSD and subsurface GSD. While both the AI and the eye observation-based assessment focus on the bed surface, the physical sampling represents a thicker layer, including the subsurface layer, too. Indeed, the so-called bed armouring phenomenon, taking place in the vicinity of the thalweg in mixed-bed rivers, leads to coarser surface grains and finer subsurface grains (see e.g., Wilcock, 2005). This may explain the case of K2 as it was located closer to the thalweg. As for the wavelet analysis-based imagery technique, an overall slight overestimation of the coarse particles can be observed, and the sand classes are, in fact, not reconstructed correctly. This finding agrees well with the field experiences of Ermilov et al. (2020), where the authors indicated the strong sensitivity of the wavelet technique on the image resolution, and showed that to detect a grain, the diameter must be at least three times larger than the pixel. In this survey, the camera was indeed closer to the riverbed at sampling



372 points K1 and K4 and the wavelet algorithm was able to detect coarse sand, but finer sand was neglected yielding
373 the lower percentages seen in Figure 8.
374



375 **Figure 8: Comparison of sediment fraction % at the sampling locations from the moving-averaged AI detection,**
376 **conventional sieving and the wavelet-based image processing method. Section K.**
377



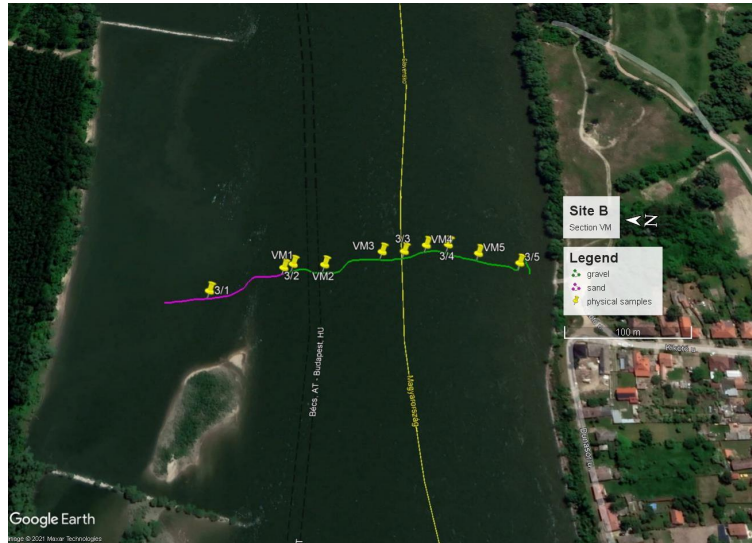
378 **Figure 9: Riverbed video images at the sampling points in Section K.**
379

380

381 At site B (Fig. 10) the river morphology is more complex compared to Site A as a groyne field is located along
382 the left bank (see again Fig. 3). As such, the low flow regions between the groynes yields the, deposition of fine
383 sediments, and much coarser bed composition in the narrowed main stream. Even though no images containing
384 only fine sediments were applied in the training phase of the AI algorithm, the model still managed to successfully

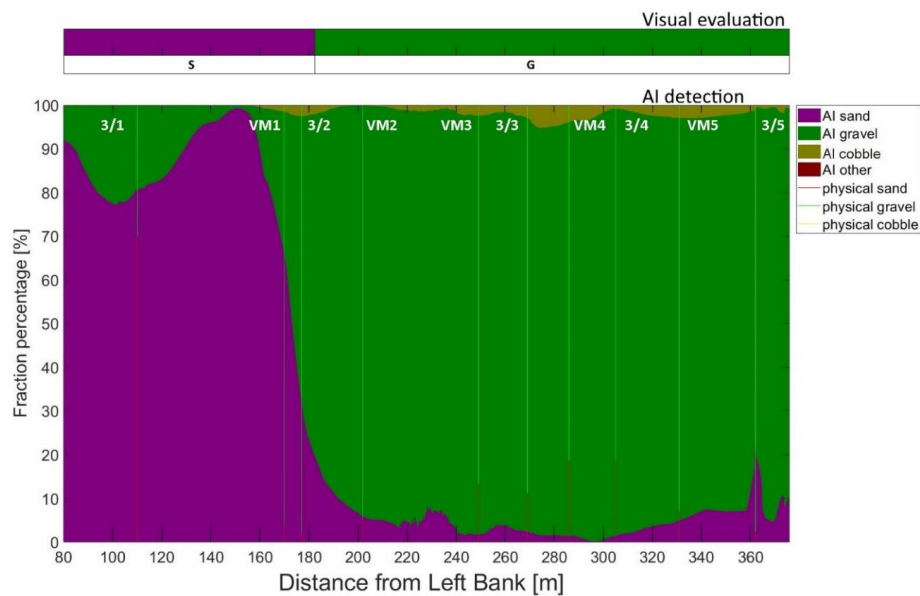


385 distinguish these zones. The fine sediments in the deposition zone at the left bank was adequately estimated and
 386 showed a good match with the visual evaluation for the whole cross-section (see Fig. 11).
 387



388
 389 **Figure 10:** The path of the vessel and camera in Section VM, Site B. The polyline is coloured based on the sediment
 390 seen during visual evaluation of the video. Yellow markers are the locations of physical bed material samplings. (Map
 391 created with © Google Earth Pro)

392



393
 394 **Figure 11:** Sediment fraction percentages in Section VM, recognised by the AI. The visual evaluation included two
 395 classes: gravel – G, sand – S). The fractions from the conventional, point samples are also shown (verticals).
 396

397



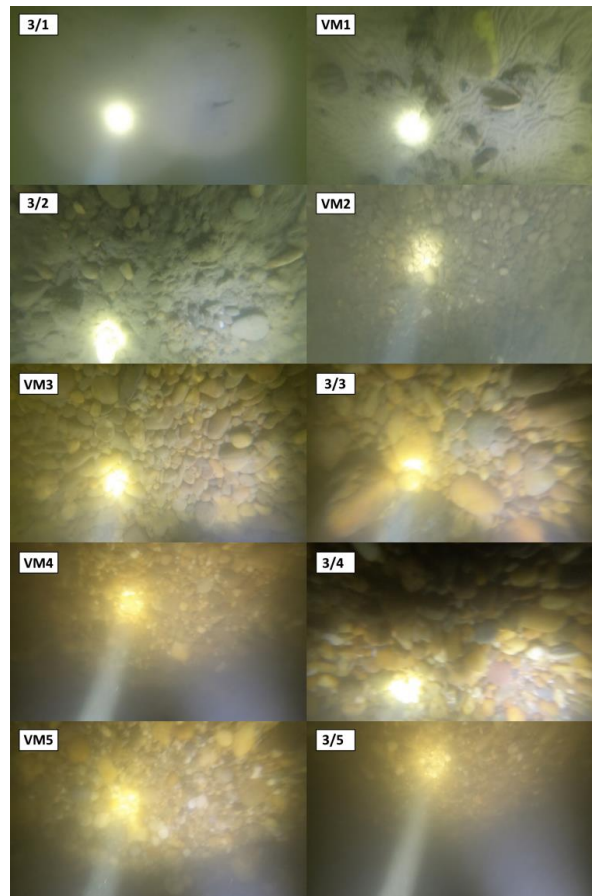
398 When comparing the AI results with the physical samples, the match is acceptable for most of the samples, such
399 as 3/1, VM2, VM3, 3/3, VM4, 3/4, VM5, respectively, with a highest difference of 10%. The significant
400 disagreements arose at sampling points VM1 and 3/2. Indeed, these points are located around the border of the of
401 the sediment deposition zone, showing steeply decreasing amount of sand moving away from the left bank (see
402 the variation from point 3/1 towards 3/2 in Fig. 12). This trend is successfully calculated by the AI algorithm, but
403 the physical samples for points VM1 and 3/2 show strong gravel dominance with negligible amount of sand (see
404 Fig. 13). Resembling the findings at the other study site, this difference can likely be explained with the disturbed
405 physical samples, which contain the sediments of the subsurface layer, too. In this case, however, the fine sediment
406 layer is accumulated on the gravel particles. It is also worth noting that the physical samples are analysed by
407 weighing the different sediment size classes, resulting in volumetric distribution. On the other hand, the imagery
408 methods provide surface distributions, hence having a thin layer of fine sediments on the top can strongly bias the
409 resulted composition (Bunte and Abt, 2001; Sime and Ferguson, 2003; Rubin et al., 2007).

410

411 At sampling point 3/5 a weaker, but still satisfactory agreement was found. Here, the AI indicated 20% sand in
412 contrast with the physical samples. Analysis of the raw videos may indicate that the suspended sediment
413 concentration was higher in this region and the transported fine particles frequently became visible passing
414 through the light beams, eventually causing disturbance in the AI analysis. Another issue in the AI algorithm was
415 associated with the illumination. As a matter of fact, a part of the images was sometimes overexposed, and the too
416 high light intensity biased the results. Examples for these problems are illustrated in Figure 14 (a: overexposure,
417 b: moving suspended sediment).

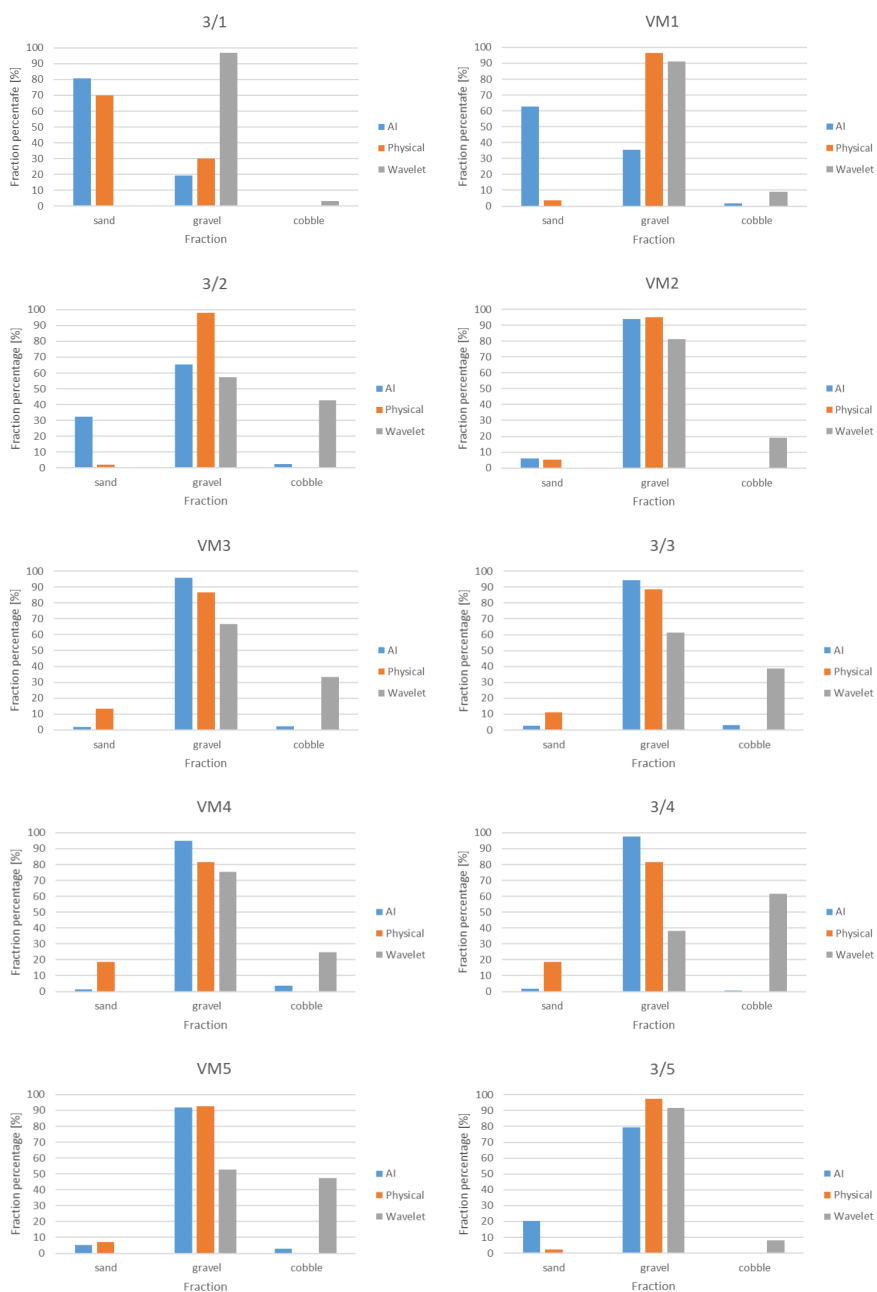
418

419 The resolution was again not sufficient for the wavelet method, and it estimated gravel and cobble regions.
420 Contrary to the previous example, it did not manage to identify coarse sand.



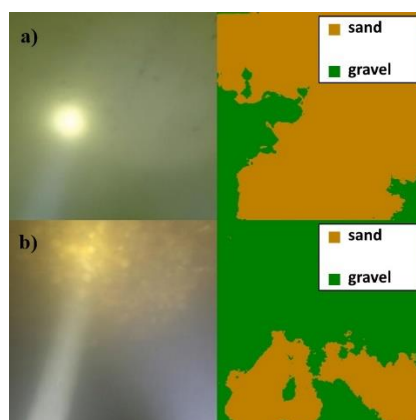
421
422

Figure 12: River bed video images at the sampling points in Section VM.



423
 424
 425

Figure 13: Comparison of sediment fraction % at the sampling locations from the moving-averaged AI detection, conventional sieving and the wavelet-based image processing method. Section VM.



426
427 **Figure 14: The effect of strong diving light on the AI algorithm in: a) purely sand covered zone and b) darker zone with**
428 **higher SSC. The original images are on the left, while the AI detections can be found on the right.**

429
430 Results of the other measurements can be found in the Appendix. Figure A2, B2 and C2 show that the trend of
431 riverbed composition from the visual evaluation is well-captured by the AI in the other cross-sections of the study
432 as well (see sampling points F/3, F/4, 1/1, 1/2 1/3, respectively). The resolution limit of the wavelet approach was
433 further noticeable (see Figure A3, B3 and C3) as it was not able to detect sand, similarly to the sampling points
434 presented earlier. In Section A, traces of possible bed armouring were found as neither the eye observation nor
435 the AI detected sand class in the images (see Figure B4) of F/1 and F/2, even though the physical samples
436 contained this fraction. In sampling point 1/4, the AI correctly detected the mixing of sand and gravel, but the
437 physical sample showed the dominance of sand rather than the gravel fraction (see Figure C3). The possible
438 explanation behind these differences resembles what was the case for the K3 sampling point, introduced earlier:
439 there was an additional finer fraction in the subsurface layer, hidden from the camera. Based on the results
440 presented in this paper, it could be established that the AI manages to recognise the main features of the riverbed
441 material composition from underwater videos with satisfactory accuracy.

442 **4.3 Implementation challenges**

443 The power supply for the entire imaging infrastructure, i.e., for the camera, the diving lights and lasers, was
444 ensured by batteries. However, due to the low temperature at the river bottom, the battery level decreased
445 extremely fast, compared to normal circumstances. Providing the power supply directly from the motorboat
446 engines can overcome this issue. To keep the camera in the adequate height also caused difficulties, since getting
447 too close to the bed can harm the devices, lifting too high, on the other hand, will result in poor image quality.
448 The measured instantaneous ADCP flow depth data was used therefore to keep the bed in camera sight, while
449 maintaining proper boat velocity to avoid blurry images. We found that a 0.2-0.45 m/s vessel speed with 60 fps
450 recording frequency was ideal to retrieve satisfactory images in a range of 0.4-1.6 m camera-bed distances. This
451 meant approximately 15 minutes long measurements per transects. Higher vessel speed caused blurred images.
452 Choosing a higher recording frequency, however, can be beneficial and alter this limitation, when provided. Lower
453 velocities could not be maintained as the river would have moved the vessel out of the section. Using a diving
454 light with small beam divergence also proved counterproductive. The high intensity, focused light occasionally
455 caused overexposed zones (white pixels) in the bed image, misleading the AI and resulting in detecting incorrect



456 classes there. The use of wide beam divergence lamps is recommended instead, with uniform light. Further
457 attention needs to be paid to the reel and its cable during the crossing when the equipment is on the upstream side
458 of the boat. If the flow velocities are relatively high (compared to the total submerged weight of the underwater
459 equipment), the cable can be pressed against the vessel-body due to the force from the flow itself, causing the reel
460 cable to jump to the side and leave its guide. This results in the equipment falling to the riverbed and the
461 measurement has to be stopped to reinstall the cable.

462
463 As for the training of the AI algorithm with the underwater images, the illumination is indeed a more crucial
464 aspect, compared to normal imagery methods. In many cases only the centre areas of the images were clearly
465 visible, whereas the remaining parts were rather dark and shady. Determining the boundaries between distinct
466 sediment classes for these images was challenging even for experienced eyes. This quality issue certainly
467 generated some incorrect annotations. To overcome this issue, manually varying the white balance thus enhancing
468 the visibility of the sediment could improve the training to some extent. It is worth noting that when Deep Learning
469 methods are to be used, most of the problems arise from the data side (Yu et al., 2007), whereas issues related to
470 the applied algorithms and hardware are rare. This is because data is more important from an accuracy perspective
471 than the actual technical infrastructure (Chen et al., 2020). The time demand of image annotation (data
472 preparation) is relatively high, i.e. an untrained person could analyse roughly 10 images per hour. On the other
473 hand, as introduced earlier, a great advantage of using AI is the capability of improving the quality of training
474 itself, often yielding better agreement with reality, compared to the manual annotation. Similar results have been
475 reported by Lu et al., (2018). This at the same time proves that there is no need for very precise manual training,
476 thus a fast and effective training process can eventually be achieved.

477
478 The validation of the Deep Learning algorithm is far from straightforward. In this study, four approaches were
479 adapted, i.e., a mathematical approach, and comparison with three other measurement methods, respectively. The
480 mathematical approach was based on calculating pixel accuracy and the Intersection-over-union parameter, as it
481 is usually done in case of Deep Learning methods to describe their efficiency (e.g. Rahman and Wang, 2016).
482 However, the latter parameter was shown to be decreased even when the model improved. Consequently, using
483 only the mathematical evaluation in this study could not describe adequately the model performance. Hence, the
484 results were compared to those of three other methods: i) visual evaluation of the image series, ii) a wavelet-based
485 image-processing method (using the method of Buscombe, 2013) and iii) riverbed composition data from physical
486 samples. Considering the features of the applied methods, the first one, i.e. the visual observation, is expected to
487 be the most suitable for the model validation. Indeed, when assessing the bed surface composition by eye, the
488 same patterns are sought, i.e. both methods focus on the uppermost sediment layer. On the other hand, the physical
489 sampling procedure inherently represents subsurface sediment layers, leading to different grain size distributions
490 in many cases. For instance, as shown above, if bed armour develops in the riverbed and the sampler breaks-up
491 this layer, the resulted sample can contain the finer particles from the subsurface layer. On the contrary, in zones
492 where a fine sediment layer is deposited on coarse grains, i.e. a sand layer on the top of a gravel bed, the physical
493 samples represent the coarse material too, moreover, considering that the sieving provides volumetric distribution
494 this sort of bias will even enhance the proportion of the coarse particles. Attempts were made to involve a third,
495 wavelet based method for model validation. However, this method failed when finer particles, i.e. sand,



496 characterized the bed. This is an inherent limitation of these type of methods, as shown already by Buscombe and
497 Masselink (2008), Cheng (2015) or Ermilov et al (2020), as the image resolution, i.e. the pixel size, is simply not
498 fine enough to reconstruct the small grain diameters in the range below fine gravel.

499

500 As it is known, the ML and DL models can learn unknown relationships in datasets, but unwanted biases as well.
501 With our current dataset, in our opinion, these biases would be the darker tones of visible grain texture and the
502 lack of larger grain sizes. This way our model in its current state is only applicable effectively in the chosen study
503 site, until the dataset is not expanded with additional images from other rivers or regions. However, the purpose
504 of the paper was to introduce the methodology itself and its potential in general and not to create a universal
505 algorithm.

506 **4.4 Novelty and future work**

507 The introduced image-based Deep Learning algorithm offers novel features in the field of sedimentation
508 engineering. First, to the authors' knowledge, underwater images of the bed of a large river have not yet been
509 analysed by AI. Second, the herein introduced method enables continuous (and quick) mapping of the riverbed,
510 in contrast to most of the earlier approaches, where only points or shorter sections were assessed with imagery
511 methods. Third, the method is much faster compared to conventional samplings or non-AI based image-processing
512 techniques. The field survey of a 400 m long transect took ~15 minutes, while the AI analysis took 4 minutes
513 (approx. 7 image/s). The speed range of 0.2-0.45 m/s of the measurement vessel and the 15 minutes per transect
514 complies with the operating protocol of general ADCP surveys on rivers (e.g., RD Instruments, 1999; Simpson,
515 2002; Mueller and Wagner, 2013). Hence, the developed image-based measurement can be carried out together
516 with the conventional boat-mounted ADCP measurements, further highlighting its time efficiency. Indeed, the
517 method is a great alternative approach for assessing riverbed material on-the-go, in underwater circumstances. As
518 a continuous and quick mapping tool, it can support other types of bed material samplings in choosing the
519 sampling locations and their optimal number. Furthermore, it can be used for quickly detecting areas of
520 sedimentation and their extent, as it was shown in Ch. 4.2. (Figure 11). This way, it may support decisions
521 regarding the maintenance of the channel or the bank-infiltrated drinking water production (detecting colmation
522 and colmated zones). Fourth, a novel approach was used for the imaging and model training. As the camera-bed
523 distance were constantly changing, the mm/pixel ratio also varied. Hence, no scale was defined for the algorithm
524 beforehand. Earlier Deep Learning methods for sediment analysis all applied fixed camera heights and/or provided
525 scaling for the AI. It should be noted that these were airborne measurements, mapping the dry zone of the rivers.
526 In an underwater manner, it is extremely challenging to keep a fixed, constant camera height due to the spatially
527 varying riverbed elevations. Hence, it is of major importance that this paper introduces a methodology and a Deep
528 Learning algorithm which neglect the need for scaling. This way, the method is faster and easier to build, but also
529 simpler to use. Of course, as a trade-off, the method, as of now, cannot reconstruct detailed grainsize distributions.
530 Indeed, the purpose was rather to provide a uniquely fast bed material mapping tool, additionally with a much
531 denser spatial resolution than the conventional methods, saving up significant resources.

532

533 Originally, beside the three main sediment grain classes introduced in the paper (sand, gravel, cobble), others were
534 also defined during annotation (e.g., bedrock, clams), but due to class imbalance (i.e., dominance of the three



535 sediment classes), these were not adapted successfully. There is a good potential in improving the method through
536 transfer learning (see Zamir et al., 2018) using broader dataset, involving other sediment types. Another possible
537 way to counter imbalance is the use of so-called weighted cross entropy (see Lu et al., 2019) on the current dataset,
538 which will also be investigated in our case.

539

540 Since the introduced method offers a quick way to provide spatially continuous bed material information of its
541 composition, it may be used to boost the training dataset of predictive, ensemble bagging-based Machine Learning
542 techniques (e.g., Ren et al., 2020) and improve their accuracy. Furthermore, the method can support the
543 implementation of other imagery techniques. For instance, using one of the training videos of this study the authors
544 managed to reconstruct the grain-scale 3D model of a riverbed section with the Structure-from-Motion technique
545 (Ermilov et al., 2020), enabling the quantitative estimation of surface roughness. Underwater field cameras can
546 also be used for monitoring and estimating bedload transport rate (Ermilov et al., 2022) by adapting LS-PIV and
547 the Statistical Background Model approach. This latter videography technique may also be used with moving
548 cameras (e.g., Hayman and Ekhlund, 2003), which enables its adaptation into our method by e.g., detecting
549 bedload movement in the cross-section.

550 5 Conclusion

551 A novel, artificial intelligence-based riverbed sediment analysis method has been introduced in this paper, which
552 uses underwater images to reconstruct the spatial variation of the characteristic sediment classes. The method was
553 trained and validated with a reasonably high number (~15000) of images, collected in a large river, in the
554 Hungarian section of the Danube. The main novelties of the developed Deep Learning based procedure are the
555 followings: i) underwater images are used, ii) the method enables continuous mapping of the riverbed along the
556 measurement vessel's route, iii) cost-efficient, iv) works without scaling, i.e., the distance between the camera
557 and the riverbed can vary. Consequently, in contrast with conventional pointwise bed sediment analysis methods,
558 this technique is robust and capable of providing continuous sediment composition data covering whole river
559 reaches, eventually providing the possibility to set up 2D bed material maps. In this way, river reach scale
560 hydromorphological assessments can be supported, where the composition of bed surface is of interest, e.g., when
561 performing habitat studies, parameterising 2D and 3D computational hydrodynamic and morphodynamic models,
562 or assessing the impact of restoration measures.

563 **Financial support.** The first author acknowledges the support of the ÚNKP-21-3 New National Excellence
564 Programme of the Ministry for Innovation and Technology, and the National Research, Development and
565 Innovation Fund, Hungary.

566 **Code availability.** The code written and used in this paper is available here: [https://bmeedu-](https://bmeedu-my.sharepoint.com/:f/g/person/ermilov_alexander_emk_bme_hu/EjL2neM4AOZGsBkYgKReViEBBzRFRFoYyLlmo6SzTB_qDQ?e=AqpqHI)
567 [my.sharepoint.com/:f/g/person/ermilov_alexander_emk_bme_hu/EjL2neM4AOZGsBkYgKReViEBBzRFRFo](https://bmeedu-my.sharepoint.com/:f/g/person/ermilov_alexander_emk_bme_hu/EjL2neM4AOZGsBkYgKReViEBBzRFRFoYyLlmo6SzTB_qDQ?e=AqpqHI)
568 [YyLlmo6SzTB_qDQ?e=AqpqHI](https://bmeedu-my.sharepoint.com/:f/g/person/ermilov_alexander_emk_bme_hu/EjL2neM4AOZGsBkYgKReViEBBzRFRFoYyLlmo6SzTB_qDQ?e=AqpqHI)



569 **Data availability.** The dataset and results can be accessed using the following link: [https://bmeedu-](https://bmeedu-my.sharepoint.com/:f/g/person/ermilov_alexander_emk_bme_hu/EhoGx64sP1tFnj8Z1OdMZA5BZWd5gDYzPyodSUDdWFjeiw?e=hKIXjq)
570 [my.sharepoint.com/:f/g/person/ermilov_alexander_emk_bme_hu/EhoGx64sP1tFnj8Z1OdMZA5BZWd5gDY](https://bmeedu-my.sharepoint.com/:f/g/person/ermilov_alexander_emk_bme_hu/EhoGx64sP1tFnj8Z1OdMZA5BZWd5gDYzPyodSUDdWFjeiw?e=hKIXjq)
571 [zPyodSUDdWFjeiw?e=hKIXjq](https://bmeedu-my.sharepoint.com/:f/g/person/ermilov_alexander_emk_bme_hu/EhoGx64sP1tFnj8Z1OdMZA5BZWd5gDYzPyodSUDdWFjeiw?e=hKIXjq)

572 **Author contributions.** GB developed the code and carried out the training process. AAE carried out the
573 fieldwork, evaluated the results, did the laboratory analysis, and collaborated with GB in improving the images.
574 SB oversaw and directed the project, while managing the financial- and equipment background.

575 **Competing interest.** The contact author has declared that none of the authors has any competing interest.

576 **Acknowledgements.** The authors would like to thank our students Dávid Koós, Gergely Tikász, Schrott Márton
577 and our technicians István Galgóczy, István Pozsgai, Károly Tóth and András Rehák for fieldwork support.

578 **References**

579 Adams, J.: Gravel Size Analysis from Photographs. *J. Hydraul. Div.*, 1979, 105, 1247–1255.
580 doi/10.1061/JYCEAJ.0005283, 1979.

581

582 Anglin, D. R., Haeseker, S. L., Skalicky, J. J., Schaller, H., Tiffan, K. F., Hatten, J. R., et al.: Effects of Hydropower
583 Operations on Spawning Habitat, Rearing Habitat, and Standing/Entrapment Mortality of Fall Chinook Salmon
584 in the Hanford Reach of the Columbia River. US Fish and Wildlife Service, final Report. Available at:
585 <https://pubs.er.usgs.gov/publication/70179516>, 2006.

586

587 Baranya, S., Fleit, G., Józsa, J., Szalóky, Z., Tóth, B., Czeglédi, I. and Erős, T.: Habitat mapping of riverine fish
588 by means of hydromorphological tools. *Ecohydrology*, Volume 11, Issue 7 e2009. Available at:
589 <https://doi.org/10.1002/eco.2009>, 2018.

590

591 Barnard, P., Rubin, D., Harney, J. and Mustain, N.: Field test comparison of an autocorrelation technique for
592 determining grain size using a digital beachball camera versus traditional methods. *Sedimentary Geology*, 201(1–
593 2): 180–195., 2007.

594

595 Benkő, G., Baranya, S., Török, T. G., and Molnár, B.: Folyami mederanyag szemösszetételének vizsgálata Mély
596 Tanulás eljárással drónfelvételek alapján (in English: Analysis of composition of river bed material with Deep
597 Learning based on drone video footages). *Hidrológiai Közlemény*, 100, 61–69., 2020.

598

599 Bovee, K. D.: A guide to stream habitat analysis using the Instream Flow Incremental Methodology. Instream
600 Flow Information, Paper no. 12., U.S.D.I. Fish and Wildlife Service, Office of Biological Services. FWS/OBS-
601 82/26. 248 pp., 1982.

602

603 Breheret, A.: Pixel Annotation Tool. Av. at: <https://github.com/abreheret/PixelAnnotationTool>, 2017.

604

605 Bunte, K. and Abt, S. R.: Sampling Surface and Subsurface Particle-Size Distributions in Wadable Gravel- and
606 Cobble-Bed Streams for Analyses in Sediment Transport, Hydraulics, and Streambed Monitoring; General
607 Technical Report (GTR), U.S. Department of Agriculture, Forest Service, Rocky Mountain Research Station: Fort
608 Collins, CO, USA, 2001.

609

610 Butler, J. B., Lane, S. N. and Chandler, J. H.: Automated extraction of grain-size data from gravel surfaces using
611 digital image processing. *J. Hydraul. Res.*, 39, 519–529., 2001.

612

613 Buscombe, D. and Masselink, G.: Grain size information from the statistical properties of digital images of
614 sediment. *Sedimentology*, 56, 421–438. doi/10.1111/j.1365-3091.2008.00977.x, 2008.

615

616 Buscombe, D.: Transferable wavelet method for grain-size distribution from images of sediment surfaces and thin
617 sections, and other natural granular patterns. *Sedimentology*, 60 1709–1732., 2013.



- 618
619 Buscombe, D., Grams, P. and Kaplinski, M.: Characterizing riverbed sediment using high-frequency acoustics: 1.
620 Spectral properties of scattering. *Journal of Geophysical Research: Earth Surface*, doi: 10.1002/2014JF003189,
621 119:12, (2674-2691), 2014a.
622
623 Buscombe, D., Grams, P. and Kaplinski, M.: Characterizing riverbed sediment using high-frequency acoustics: 2.
624 Scattering signatures of Colorado River bed sediment in Marble and Grand Canyons. *Journal of Geophysical*
625 *Research: Earth Surface*, doi/full/10.1002/2014JF003191, 119:12, (2674-2691), 2014b.
626
627 Buscombe, D. and Ritchie, A. C.: Landscape Classification with Deep Neural Networks. *Geosciences*, 8, 244.
628 Available at: <https://doi.org/10.3390/geosciences8070244>, 2018.
629
630 Buscombe, D.: SediNet: a configurable deep learning model for mixed qualitative and quantitative optical
631 granulometry optical granulometry. *Earth Surface Processes and Landforms*, 45, 638-651. DOI:
632 10.1002/esp.4760, 2020.
633
634 Butler, J. B., Lane, S. N. and Chandler, J. H.: Automated extraction of grain-size data from
635 gravel surfaces using digital image processing. *J. Hydraul. Res.* 2001, 39, 519-529. Available at:
636 <https://doi.org/10.1080/00221686.2001.9628276>, 2001.
637
638 Carbonneau, P. E., Lane, S. N and Bergeron, N. E.: Catchment-scale mapping of surface grain size in gravel bed
639 rivers using airborne digital imagery. *Water Resources Research*, 40(7): W07202., 2004.
640
641 Chandler, J., Lane, S. N. and Ashmore, P.: Measuring river-bed and flume morphology and parameterising bed
642 roughness with a KODAK DCS460 digital camera. *International Archives of Photogrammetry and Remote*
643 *Sensing*, Vol. XXXIII, Part B7., 2000.
644
645 Chen, C., Zhang, P., Zhang, H., Dai, J., Yi, Y., Zhang, H. and Zhang, Y.: Deep Learning on Computational-
646 Resource-Limited Platforms: A Survey. Volume 2020, Article ID 8454327. Available at:
647 <https://doi.org/10.1155/2020/8454327>, 2020.
648
649 Chen, L., Zhu, Y., Isola, P., Papandreou, G., Schroff, F. and Adam, H.: Encoder-Decoder with Atrous Separable
650 Convolution for Semantic Image Segmentation. *Proceedings of the European conference on computer vision*
651 (ECCV) (pp. 801-818). <https://arxiv.org/abs/1802.02611>, 2018.
652
653 Cheng, D., Li, X., Li, W. H., Lu, C., Li, F., Zhao, H. and Zheng, W. S.: Large-Scale Visible Watermark Detection
654 and Removal with Deep Convolutional Networks. In book: *Pattern Recognition and Computer Vision. First*
655 *Chinese Conference, PRCV, Guangzhou, China, Proceedings, Part III*. DOI: 10.1007/978-3-030-03338-5_3,
656 2018.
657
658 Cheng, Z., and Liu, H.: Digital grain-size analysis based on autocorrelation algorithm. *Sedimentary Geology*, 327,
659 21-31. Available at: <https://doi.org/10.1016/j.sedgeo.2015.07.008>, 2015.
660
661 Chezar, H. and Rubin, D. M.: Underwater Microscope System. United States Patent Office, The United States of
662 America as represented by the Secretary of the Interior, US Patent No. 6,680,795 B2., 2004.
663
664 Church, M. A., McLean, D. G., and Wolcott, J. F.: *Sediments transport in Gravel Bed Rivers*. Chap.: *River Bed*
665 *Gravels: Sampling and Analysis*. John Wiley and Sons, New York, 43–88, 1987.
666
667 Delong, M. D. and Brusven, M. A.: Classification and spatial mapping of riparian habitat with applications toward
668 management of streams impacted by nonpoint source pollution. *Environmental Management*, 15:565-571. DOI:
669 10.1007/BF02394745, 1991.
670
671 Detert, M. and Weitbrecht, V.: User guide to gravelometric image analysis by BASEGRAIN. In *Advances in*
672 *Science and Research; Fukuoka, S., Nakagawa, H., Sumi, T., Zhang, H., Eds.; Taylor and Francis Group: London,*
673 *UK, 2013; pp. 1789–1795. ISBN 978-1-138-00062-9.*, 2013.
674
675 Diplas, P.: Sampling Techniques for Gravel Sized Sediments. *Journal of Hydraulic Engineering*. DOI:
676 10.1061/(ASCE)0733-9429(1988)114:5(484), 1988.
677



- 678 Ermilov, A.A., Baranya, S. and Török, G.T.: Image-Based Bed Material Mapping of a Large River. *Water*, 12,
679 916. Available at: <https://doi.org/10.3390/w12030916>, 2020.
680
- 681 Ermilov, A. A., Fleit, G., Conevski, S., Guerrero, M., Baranya, S., & Rütther, N.: Bedload transport analysis using
682 image processing techniques. *ACTA GEOPHYSICA*, 1895-6572 1895-7455. [http://doi.org/10.1007/s11600-022-](http://doi.org/10.1007/s11600-022-00791-x)
683 00791-x, 2022.
684
- 685 Fehr, R.: Einfache Bestimmung der Korngrößenverteilung von Geschiebematerial mit Hilfe der
686 Linienzahlanalyse (In English: Simple detection of grain size distribution of sediment material using line-count
687 analysis). *Schweizer Ing. und Archit.*, 105, 1104–1109., 1987.
688
- 689 Fetzer, J., Holzner, M., Plötze, M. and Furrer, G.: Clogging of an Alpine streambed by silt-sized particles –
690 Insights from laboratory and field experiments. *Water Research*, Volume 126, Pages 60-69.
691 <https://doi.org/10.1016/j.watres.2017.09.015>, 2017.
692
- 693 Geist, D. R., Jones, J., Murray, C. J. and Dauble, D. D.: Suitability criteria analyzed at the spatial scale of redd
694 clusters improved estimates of fall chinook salmon (*Oncorhynchus tshawytscha*) spawning habitat use in the
695 Hanford Reach, Columbia River. *Canadian Journal of Fisheries and Aquatic Sciences*, 57: 1636-1646., 2000.
696
- 697 Gilcher, M. and Udelhoven, T.: Field Geometry and the Spatial and Temporal Generalization of Crop
698 Classification Algorithms—A Randomized Approach to Compare Pixel Based and Convolution Based Methods.
699 *Remote Sens.*, 13, 775., 2021.
700
- 701 GOPRO Hero 4 Silver: User Manual. Available at: [https://gopro.com/content/dam/help/hero4-](https://gopro.com/content/dam/help/hero4-silver/manuals/UM_H4Silver_ENG_REVA_WEB.pdf)
702 [silver/manuals/UM_H4Silver_ENG_REVA_WEB.pdf](https://gopro.com/content/dam/help/hero4-silver/manuals/UM_H4Silver_ENG_REVA_WEB.pdf), 2014.
703
- 704 GOPRO Hero 7 Black: User Manual. Available at: [https://gopro.com/content/dam/help/hero7-](https://gopro.com/content/dam/help/hero7-black/manuals/HERO7Black_UM_ENG_REVA.pdf)
705 [black/manuals/HERO7Black_UM_ENG_REVA.pdf](https://gopro.com/content/dam/help/hero7-black/manuals/HERO7Black_UM_ENG_REVA.pdf), 2018.
706
- 707 Graham, D. J., Reid, I. and Rice, S. P.: Automated sizing of coarse-grained sediments: image-processing
708 procedures. *Mathematical Geology*, 37, 1–28. <https://doi.org/10.1007/s11004-005-8745-x>, 2005.
709
- 710 Graham, D. J. Rollet, A.J., Piégay, H. and Rice, S. P.: Maximizing the accuracy of image-based surface sediment
711 sampling techniques. *Water Resour. Res.*, 46, W02508. [https://doi.org/](https://doi.org/10.1029/2008WR006940)
712 [10.1029/2008WR006940](https://doi.org/10.1029/2008WR006940), 2010.
713
- 714 Grams, P. E., Topping, D. J., Schmidt, J. C., Hazel, J. E. and Kaplinski, M.: Linking morphodynamic response
715 with sediment mass balance on the Colorado River in Marble Canyon: Issues of scale, geomorphic setting, and
716 sampling design. *J. Geophys. Res. Earth Surf.*, 118, 361–381, doi:10.1002/jgrf.20050., 2013.
717
- 718 Guerit, L., Barrier, L., Liu, Y., Narteau, C., Lajeunesse, E., Gayer, E., Métivier, F.: Uniform grain-size distribution
719 in the active layer of a shallow, gravel-bedded, braided river (the Urumqi River, China) and implications for paleo-
720 hydrology. *Earth Surface Dynamics*. 6. 1011-1021. DOI: 10.5194/esurf-6-1011-2018., 2018.
721
- 722 Guerrero, M. and Lamberti, A.: Flow field and morphology mapping using ADCP and multibeam techniques:
723 Survey in the Po River. *J. Hydraul. Eng.*, 137, 1576–1587, doi:10.1061/
724 (ASCE)HY.1943-7900.0000464., 2011.
725
- 726 Guerrero, M., Rütther, N., Szupiany, R., Haun, S., Baranya, S. and Latosinski, F.: The Acoustic Properties of
727 Suspended Sediment in Large Rivers: Consequences on ADCP Methods Applicability. *Water*, 8, 13;
728 doi:10.3390/w8010013, 2016.
729
- 730 Haddadchi, A., Booker, D.J. and Measures, R.J.: Predicting river bed substrate cover proportions across New
731 Zealand. *Catena*, Volume 163, pp. 130-146. Available at: <https://doi.org/10.1016/j.catena.2017.12.014>, 2018.
732
- 733 Hayman, E., Eklundh, J.: Statistical Background Subtraction for a Mobile Observer. Proceedings of the Ninth
734 IEEE International Conference on Computer Vision (ICCV 2003) 2-Volume Set 0–7695–1950–4/03, 2003.
735



- 736 Ibbeken, H., and Schleyer, R.: Photo-sieving: A method for grain-size analysis of coarse-grained, unconsolidated
737 bedding surfaces. *Earth Surf. Process. Landforms*, 11, 59–77. Available at:
738 <https://doi.org/10.1002/esp.3290110108>, 1986.
739
- 740 Igathinathane, C., Melin, S., Sokhansanj, S., Bi, X., Lim, C. J., Pordesimo, L. O. and Columbus, E. P.: Machine
741 vision based particle size and size distribution determination of airborne dust particles of wood and bark pellets.
742 *Powder Technol.*, 196, 202–212. Available at: <https://doi.org/10.1016/j.powtec.2009.07.024>, 2009.
743
- 744 Kellerhals, R. and Bray, D. I.: Sampling Procedures for Coarse Fluvial Sediments. *J. Hydraul. Div.*, 97, 1165–
745 1180., 1971.
746
- 747 Kim, H., Han, J. and Han, T. Y.: Machine vision-driven automatic recognition of particle size and morphology in
748 SEM images. *Nanoscale*, 12, 19461–19469. Available at: <https://doi.org/10.1039/D0NR04140H>, 2020.
749
- 750 Le, Q. V.: Building high-level features using large scale unsupervised learning. In Proceedings of the 2013 IEEE
751 International Conference on Acoustics, Speech and Signal Processing, Vancouver, BC, Canada, pp. 8595–8598.,
752 2013.
753
- 754 Leopold, L. B.: An Improved Method for Size Distribution of Stream Bed Gravel. *Water Resour. Res.*, 6, 1357–
755 1366. <https://doi.org/10.1029/WR006i005p01357>, 1970.
756
- 757 Limare, A., Tal, M., Reitz, M. D., Lajeunesse, E., and Métivier, F.: Optical method for measuring bed topography
758 and flow depth in an experimental flume. *Solid Earth*, 2, 143–154, <https://doi.org/10.5194/se-2-143-2011>, 2011.
759
- 760 Lowe, D. G.: Distinctive Image Features from Scale-Invariant Keypoints. *International Journal of Computer*
761 *Vision*, 60, pages 91–110, 2004.
762
- 763 Lu, S., Gao, F., Piao, Ch. and Ma, Y.: Dynamic Weighted Cross Entropy for Semantic Segmentation with
764 Extremely Imbalanced Data. 2019 International Conference on Artificial Intelligence and Advanced
765 Manufacturing (AIAM). doi: 10.1109/AIAM48774.2019.00053, 2019.
766
- 767 Mueller D. S., Wagner, Ch. R.: Measuring Discharge with Acoustic Doppler Current Profilers from a Moving
768 Boat. USGS, Chapter 22 of Book 3, Section A. <https://pubs.usgs.gov/tm/3a22/>, 2009.
769
- 770 Mueller D. S., Wagner, Ch. R.: Measuring discharge with acoustic Doppler current profilers from a moving boat,
771 version 2.0. [https://www.researchgate.net/publication/284587353_Measuring_discharge_with_acoustic_-_](https://www.researchgate.net/publication/284587353_Measuring_discharge_with_acoustic_-_Doppler_current_profilers_from_a_moving_boat)
772 [Doppler current profilers from a moving boat](https://www.researchgate.net/publication/284587353_Measuring_discharge_with_acoustic_-_Doppler_current_profilers_from_a_moving_boat), 2013.
773
- 774 Muste, M., Baranya, S., Tsubaki, R., Kim, D., Ho, H., Tsai, H. and Law, D.: Acoustic mapping velocimetry. *Water*
775 *Resour. Res.*, 52, 4132–4150, doi:10.1002/2015WR018354., 2016.
776
- 777 Obodovskyi, O., Habel, M., Szatten, D., Rozlach, Z., Babiński, Z., Maerker, M.: Assessment of the Dnieper
778 Alluvial Riverbed Stability Affected by Intervention Discharge Downstream of Kaniv Dam. *Water*, 12(4):1104.
779 <https://doi.org/10.3390/w12041104>, 2020.
780
- 781 Padilla, R., Netto, S. M. and da Silva, E. A. B.: A Survey on Performance Metrics for Object-Detection
782 Algorithms. Conference: 2020 International Conference on Systems, Signals and Image Processing (IWSSIP).
783 DOI: 10.1109/IWSSIP48289.2020, 2020.
784
- 785 Perez, L. and Wang, J.: The Effectiveness of Data Augmentation in Image Classification using Deep Learning.
786 arXiv preprint arXiv:1712.04621. Av. at: <https://arxiv.org/abs/1712.04621>. 2017., 2017.
787
- 788 Purinton, B. and Bookhagen, B.: Introducing PebbleCounts: A grain-sizing tool for photo surveys of dynamic
789 gravel-bed rivers. *Earth Surf. Dyn.*, 7, 859–877. <https://doi.org/10.5194/esurf-7-859-2019>, 2019.
790
- 791 Rákóczi, L.: Selective erosion of noncohesive bed materials. *Geografiska Annaler. Series A, Physical Geography*,
792 Vol. 69, No. 1, pp. 29-35. <https://doi.org/10.2307/521364>, 1987.
793
- 794 Rákóczi, L.: Identification of river channel areas inclined for colmation, based on the analysis of bed material.
795 *Vízügyi Közlemények, LXXIX.*, chapter 3., 1997.



- 796
797 Rahman, M. A. and Wang, Y.: Optimizing Intersection-Over-Union in Deep Neural Networks for Image
798 Segmentation. In: Bebis G. et al. (eds) Advances in Visual Computing. ISVC 2016. Lecture Notes in Computer
799 Science, vol 10072. Springer, Cham. https://doi.org/10.1007/978-3-319-50835-1_22, 2016.
800
801 RD Instruments – Acoustic Doppler Current Profilers – Application Note: https://www.commtec.com/library/Technical_Papers/RDI/FSA-004%20Model.pdf, 1999.
802
803
804 Rice, S. and Church, M.: Grain size along two gravel-bed rivers: Statistical variation, spatial pattern and
805 sedimentary links. *Earth Surf. Process. Landf.*, 23, 345–363., 1998.
806
807 Ren, H., Hou, Z., Duan, Z., Song, X., Perkins, W. A., Richmond, M. C., Arntzen, E. V. and Scheibe, T. D.: Spatial
808 Mapping of Riverbed Grain-Size Distribution Using Machine Learning. *Front. Water*, 2:551627. doi:
809 10.3389/frwa.2020.551627, 2020.
810
811 Rozniak, A., Schindler, K., Wegner, J. D. and Lang, N.: Drone images and Deep Learning for river monitoring in
812 Switzerland. Semester project. Institute of Geodesy and Photogrammetry, Project, Swiss Federal Institute of
813 Technology (ETH) Zurich, 2019.
814
815 Rubin, D. M.: A simple autocorrelation algorithm for determining grain-size from digital images of sediment. *J.*
816 *Sed. Res.*, 74, 160–165., 2004.
817
818 Rubin, D. M., Chezard, H., Harney, J. N., Topping, D. J., Melis, T. S., Sherwood, C. R.: Underwater microscope
819 for measuring spatial and temporal changes in bed-sediment grain size. *Sedimentary Geology*, Volume 202, Issue
820 3, Pages 402-408, <https://doi.org/10.1016/j.sedgeo.2007.03.020>, 2007.
821
822 Scheder, C., Lerchegger, B., Flödl, P., Csar, D., Gumpinger, C. and Hauer, C.: River bed stability versus clogged
823 interstitial: Depth-dependent accumulation of substances in freshwater pearl mussel (*Margaritifera margaritifera*
824 L.) habitats in Austrian streams as a function of hydromorphological parameters. *Limnologia*, Volume 50,
825 January 2015, Pages 29-39. <https://doi.org/10.1016/j.limno.2014.08.003>, 2015.
826
827 Shields, F. D., Jr. and Rigby, J. R.: River habitat quality from river velocities measured using acoustic Doppler
828 current profiler. *Environ. Manage.*; 36(4):565-75. doi: 10.1007/s00267-004-0292-6., 2005.
829
830 Shields, F. D. Jr.: Aquatic Habitat Bottom Classification Using ADCP. *Journal of Hydraulic Engineering*, Vol.
831 136, Issue 5, 2010.
832
833 Sime, L. C. and Ferguson, R. I.: Information on grain-sizes in gravel bed rivers by automated image analysis. *J.*
834 *Sed. Res.*, 73, 630–636., 2003.
835
836 Simpson, M. R.: Discharge Measurements Using a Broad-Band Acoustic Doppler Current Profiler. USGS, Open-
837 File Report 01-1, <https://pubs.usgs.gov/of/2001/ofr0101/>, 2002.
838
839 Singer, M. B.: A new sampler for extracting bed material sediment from sand and gravel beds in navigable rivers.
840 *Earth Surface Processes and Landforms* 33(14):2277 – 2284 DOI: 10.1002/esp.1661, 2008.
841
842 Soloy, A., Turki, I., Fournier, M., Costa, S., Peuziat, B. and Lecoq, N.: A Deep Learning-Based Method for
843 Quantifying and Mapping the Grain Size on Pebble Beaches. *Remote Sens.*, 12, 3659, doi:10.3390/rs12213659,
844 2020.
845
846 Staudt, F., Mullarney, J. C., Pilditch, C. A. and Huhn, K.: Effects of grain-size distribution and shape on sediment
847 bed stability, near-bed flow and bed microstructure. *Earth Surface Processes and Landforms*, 44(5). DOI:
848 10.1002/esp.4559, 2018.
849
850 Sun, Z., Zheng, H. and Sun, L.: Analysis on the Characteristics of Bed Materials in the Jinghong Reservoir on the
851 Lancang River. *Sustainability*, 13, 6874. <https://doi.org/10.3390/su13126874>, 2021.
852
853 Takechi, H., Aragaki, S. and Irie, M.: Differentiation of River Sediments Fractions in UAV Aerial Images by
854 Convolution Neural Network. *Remote Sens.*, 13, 3188. <https://doi.org/10.3390/rs13163188>, 2021.
855



- 856 Taravat, A., Wagner, M. P., Bonifacio, R. and Petit, D.: Advanced Fully Convolutional Networks for Agricultural
857 Field Boundary Detection. *Remote Sens.*, 13, 722., 2021.
858
- 859 Török, G. T., Baranya, S. (2017) Morphological Investigation of a Critical Reach of the Upper Hungarian Danube.
860 *Periodica Polytechnica Civil Engineering*. 61(4), pp. 752–761. <https://doi.org/10.3311/PPci.10530>, 2017.
861
- 862 Török, G. T., Baranya, S. and Rütther, N.: 3D CFD Modeling of Local Scouring, Bed Armoring and Sediment
863 Deposition. *Water*, 9(1), 56, <https://doi.org/10.3390/w9010056>, 2017.
864
- 865 USDA: Guidelines for Sampling Bed Material. Technical Supplement 13A, 2007.
866
- 867 Vanoni, V. A. and Hwang, L. S.: Relation between Bed Forms and Friction in Streams. *J. Hydraulics Division.*,
868 93 (3), 121–144. doi:10.1061/JYCEAJ.0001607, 1967.
869
- 870 Verdú, J. M., Batalla, R. J. and Martínez-Casanovas, J. A.: High-resolution grain-size characterisation of gravel
871 bars using imagery analysis and geo-statistics. *Geomorphology*, 72, 73–93., 2005.
872
- 873 Warrick, J. A., Rubin, D. M., Ruggiero, P., Harney, J. N., Draut, A. E. and Buscombe, D.: Cobble cam: Grain-
874 size measurements of sand to boulder from digital photographs and autocorrelation analyses. *Earth Surf. Process*
875 *Landf.*, 34, 1811–1821. <https://doi.org/10.1002/esp.1877>, 2009.
876
- 877 Wilcock, P. R.: Persistence of armor layers in gravel-bed streams. *Hydrology and Land Surface Studies*.
878 <https://doi.org/10.1029/2004GL021772>, 2005.
879
- 880 Wolcott, J. F., Church, M.: Strategies for sampling spatially heterogeneous phenomena: The example of river
881 gravels. *Journal of Sedimentary Research*. v. 61, no. 4, p. 534–543, 1991.
882
- 883 WMO: Measurement of river sediments: prepared by the Rapporteur on Sediment Transport of the Commission
884 for Hydrology. Report, World Meteorological Organization - No. 561, Operational hydrology report (OHR)- No.
885 16, 1981.
886
- 887 Yang, F., Yi, M., Cai, Y., Blasch, E., Sullivan, N., Sheaff, C., Chen, G. and Ling, H.: Multitask Assessment of
888 Roads and Vehicles Network (MARVN). *Proceedings Volume 10641, Sensors and Systems for Space*
889 *Applications XI*, 106410D, <https://doi.org/10.1117/12.2305972>, 2018.
890
- 891 Yu, L., Wang, S. and Lai, K.K.: Data Preparation in Neural Network Data Analysis. In book: *Foreign-Exchange-*
892 *Rate Forecasting with Artificial Neural Networks*. DOI: 10.1007/978-0-387-71720-3_3, 2007.
893
- 894 Zamir, A. R., Sax, A., Shen, W., Guibas, L., Malik, J. and Savarese, S.: Taskonomy: Disentangling Task Transfer
895 Learning. In *Proceedings of the 2018 IEEE/CVF Conf. on Computer Vision and Pattern Recognition*, Salt Lake
896 City, UT, USA, pp. 3712–3722. doi: 10.1109/CVPR.2018.00391, 2018.
897
- 898 Zhang, Q., Shi, Y., Chen, Z. and Jiang, T.: ADCP measured flow current of the middle-lower Changjiang River
899 channel. *Front. Earth Sci., China* 2, 1–9. <https://doi.org/10.1007/s11707-008-0016-y>, 2008.
900
- 901 Zhou, Y., Lu, J., Jin, Z., Li, Y., Gao, Y., Liu, Y. and Chen, P.: Experimental Study on the Riverbed Coarsening
902 Process and Changes in the Flow Structure and Resistance in the Gravel Riverbed Downstream of Dams. *Front.*
903 *Environ. Sci.*, <https://doi.org/10.3389/fenvs.2021.611668>, 2021.
904
- 905 Zhu, J., Park, T., Isola, P. and Efros, A. A.: Unpaired Image-to-Image Translation using Cycle-Consistent
906 Adversarial Networks. *arxiv*, <https://arxiv.org/abs/1703.10593>, 2020.
907



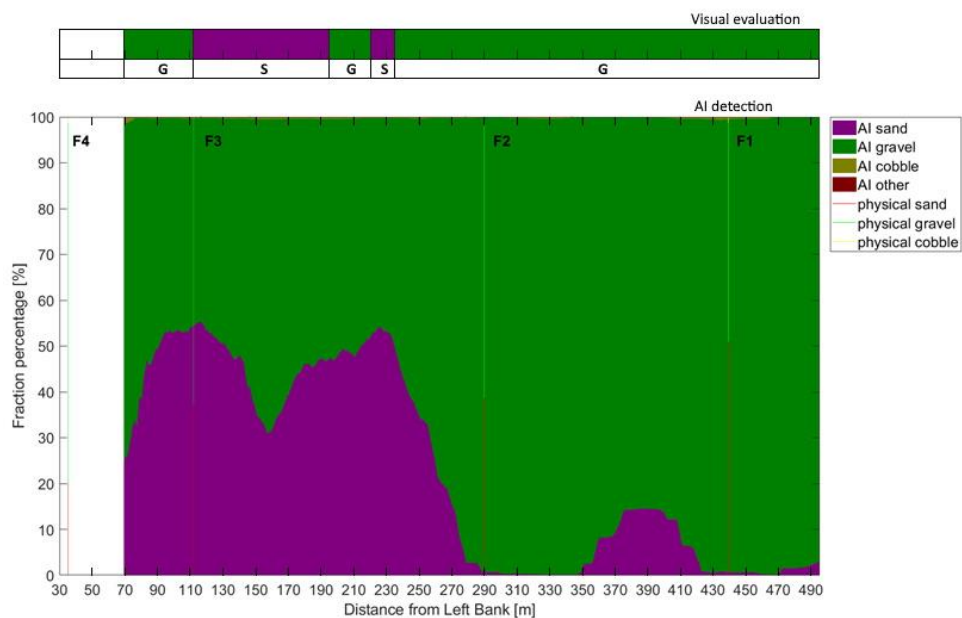
908 **Appendix**

909 **Appendix A Site A - Section F**



910
 911 **Figure A1:** The path of the vessel and camera in Section F, Site A. The polyline is coloured based on the sediment seen
 912 during visual evaluation of the video. Yellow markers are the locations of physical bed material samplings. (Map
 913 created with © Google Earth Pro)

914

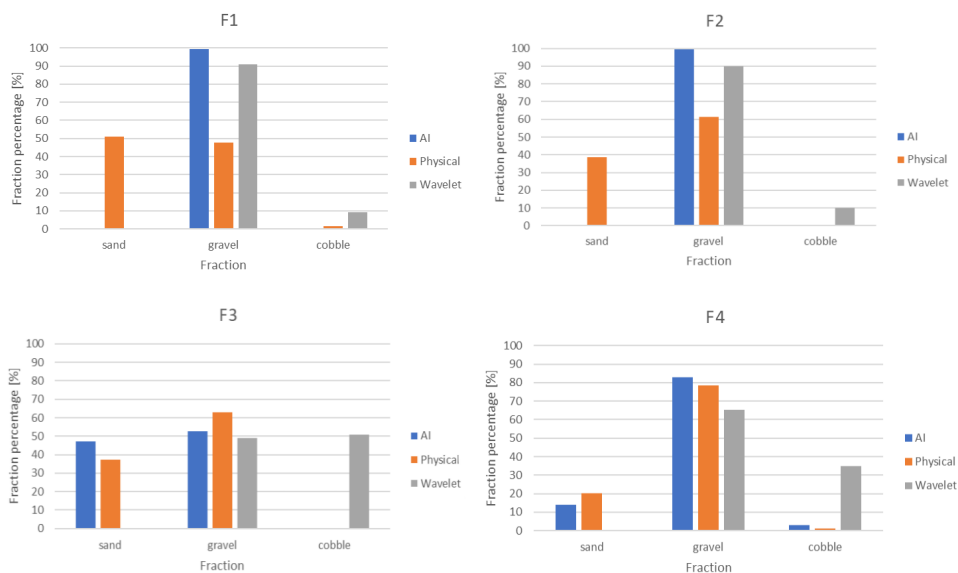


915
 916 **Figure A2:** Sediment fraction percentages in Section F, recognised by the AI. The visual evaluation included two classes:
 917 gravel – G, sand – S). The fractions from the physical samples are also shown (verticals).



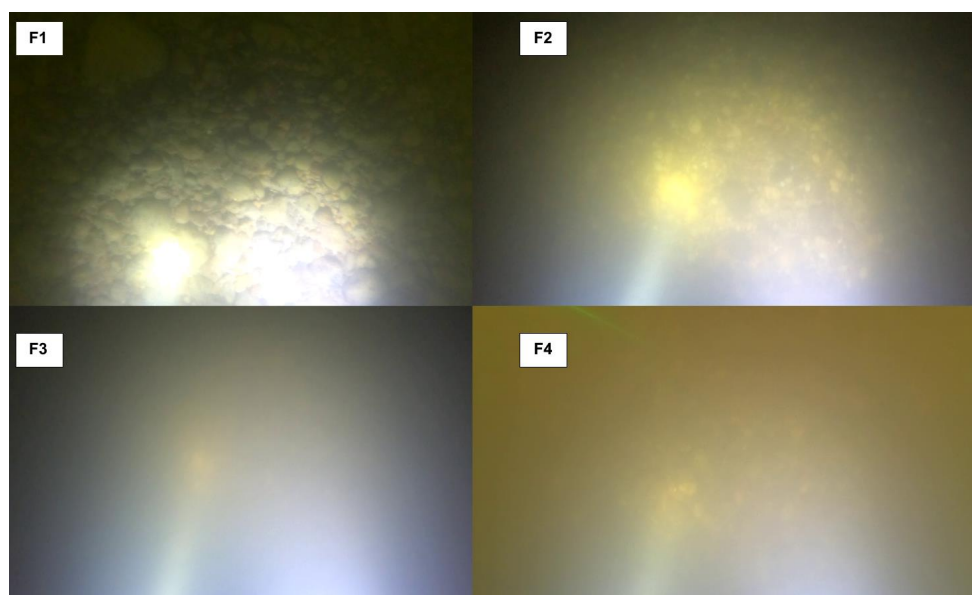
918

919



920
 921
 922

Figure A3: Comparison of sediment fraction % at the sampling locations from the moving-averaged AI detection, conventional sieving and the wavelet-based image processing method. Section F.



923
 924

Figure A4: Riverbed video images at the sampling points in Section F.

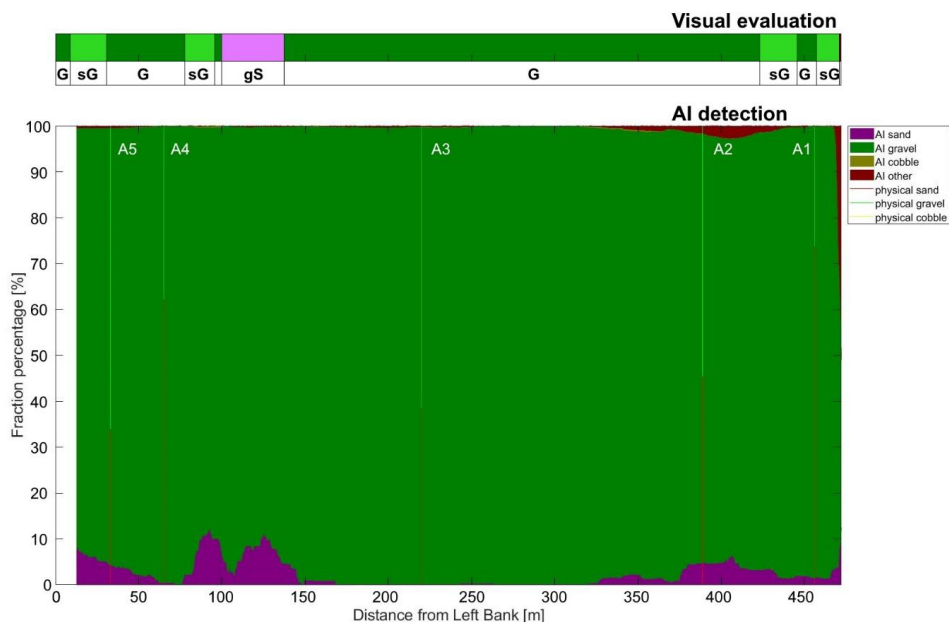


925 Appendix B Site A – Section A

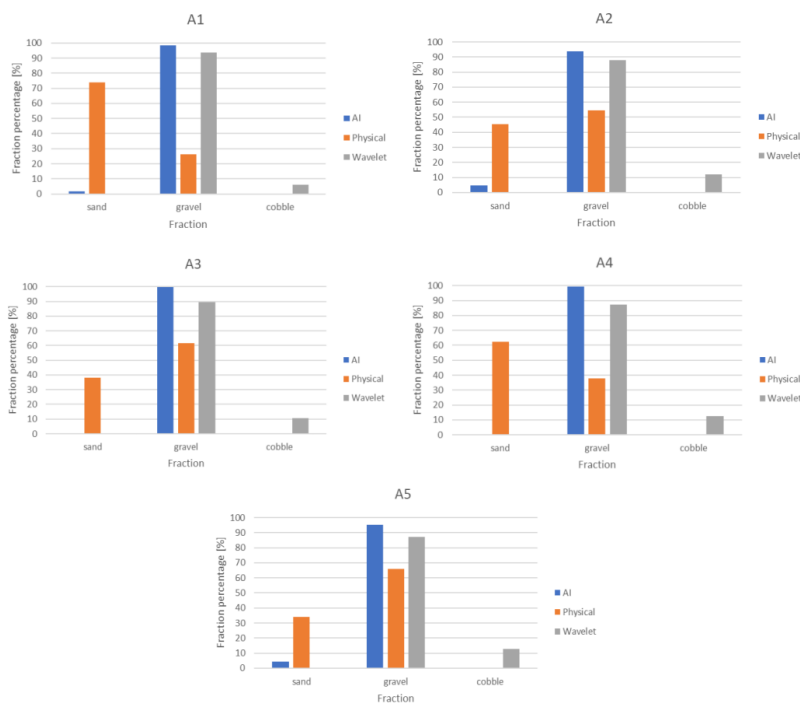


926
 927 **Figure B1:** The path of the vessel and camera in Section A, Site A. The polyline is coloured based on the sediment seen
 928 during visual evaluation of the video. Yellow markers are the locations of physical bed material samplings. (Map
 929 created with © Google Earth Pro)

930

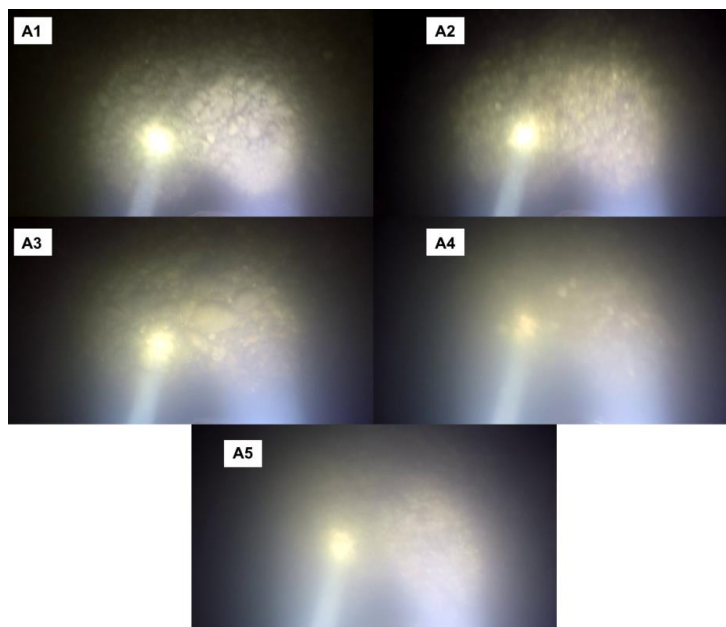


931
 932 **Figure B2:** Sediment fraction percentages in Section A, recognised by the AI. The visual evaluation included three
 933 classes: gravel – G, sandy gravel – sG, gravelly sand - gS). The fractions from the physical samples are also shown
 934 (verticals).



935
936
937

Figure B3: Comparison of sediment fraction % at the sampling locations from the moving-averaged AI detection, conventional sieving and the wavelet-based image processing method. Section A.



938
939
940

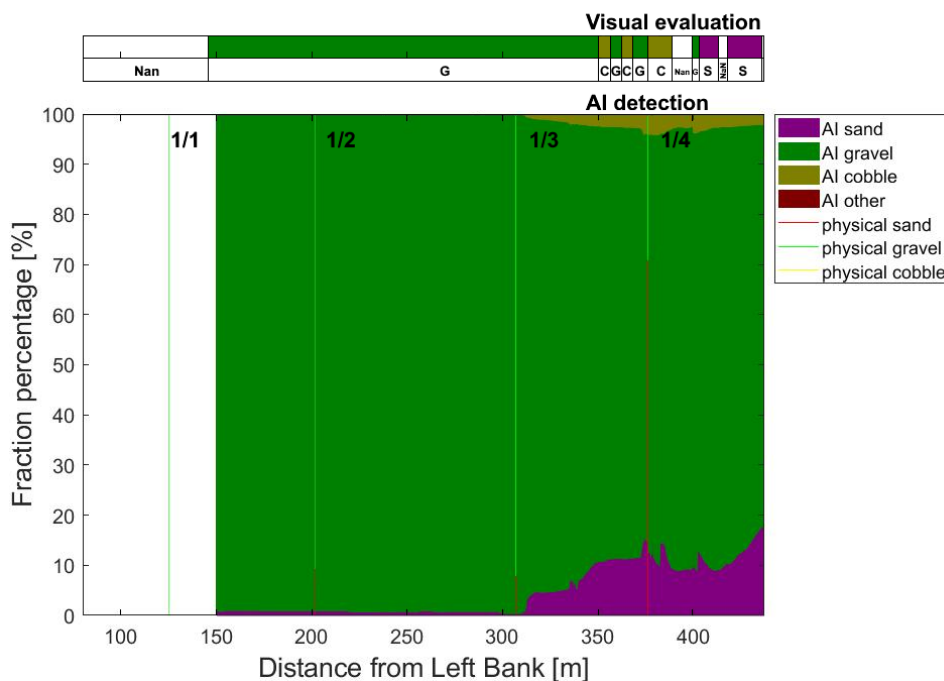
Figure B4: Riverbed video images at the sampling points in Section A.



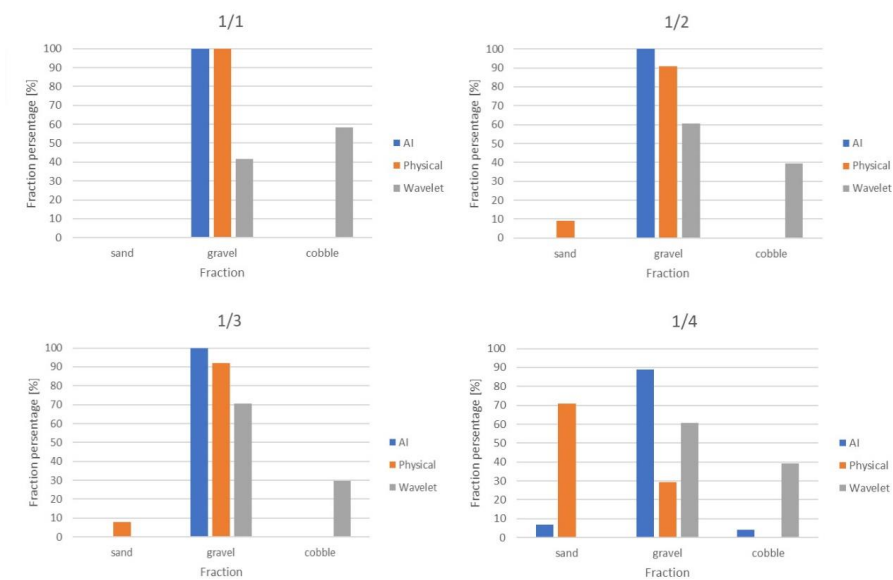
941 Appendix C Site B – Section NY



942
 943 Figure C1: The path of the vessel and camera in Section NY, Site B. The polyline is coloured based on the sediment
 944 seen during visual evaluation of the video. Yellow markers are the locations of physical bed material samplings. (Map
 945 created with © Google Earth Pro)

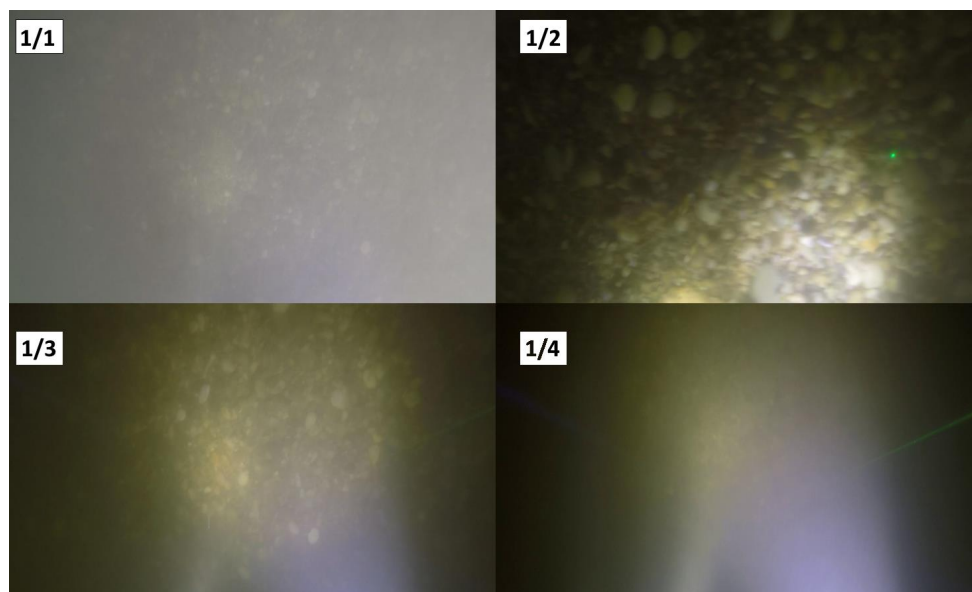


946
 947 Figure C2: Sediment fraction percentages in Section NY, recognised by the AI. The visual evaluation included two
 948 classes: gravel – G, sand – S). The fractions from the physical samples are also shown (verticals).



949
 950
 951

Figure C3: Comparison of sediment fraction % at the sampling locations from the moving-averaged AI detection, conventional sieving and the wavelet-based image processing method. Section NY.



952
 953

Figure C4: River bed video images at the sampling points in Section NY.